MICROCOPY RESOLUTION TEST CHART

NATIONAL BUREAU OF STANDARDS 1963-A

AD A139946

RADC-TR-83-243
Final Technical Report
November 1983

DEVELOPMENT OF NEW ELECTRO-OPTIC AND ACOUSTO-OPTIC MATERIALS

Hughes Research Laboratories
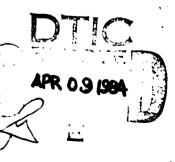
N. R. Kyle
R. R. Stephens
M. E. Pedinoff
S. R. Sashital
A. L. Gentile
J. F. Lotspeich

APPROVED FOR PUBLIC RELEASE; DISTRIBUTION UNLIMITED

ROME AIR DEVELOPMENT CENTER
Air Force Systems Command
Griffiss Air Force Base, NY 13441

DTIC
APR 09 1984

DTIC FILE COPY

84 04 06 011

This report has been reviewed by the RADC Public Affairs Office (PA) and is releasable to the National Technical Information Service (NTIS). At NTIS it will be releasable to the general public, including foreign nations.

RADC-TR-83-243 has been reviewed and is approved for publication.

APPROVED:

JOHN J. LARKIN
Project Engineer

APPROVED:

HAROLD ROTH
Director, Solid State Sciences Division

FOR THE COMMANDER:

JOHN A. RITZ
Acting Chief, Plans Office

REPORT DOCUMENTATION PAGE		READ INSTRUCTIONS BEFORE COMPLETING FORM
1. REPORT NUMBER RADC-TR-83-243	2. GOVT ACCESSION NO. AD-A139946	3. RECIPIENT'S CATALOG NUMBER
4. TITLE *(and Subtitle)* DEVELOPMENT OF NEW ELECTRO-OPTIC AND ACOUSTO-OPTIC MATERIALS		5. TYPE OF REPORT & PERIOD COVERED Final Technical Report 1 Apr 81 – 31 Mar 83
		6. PERFORMING ORG. REPORT NUMBER N/A
7. AUTHOR(s) N. R. Kyle S. R. Sashital R. R. Stephens A. L. Gentile M. E. Pedinoff J. F. Lotspeich		8. CONTRACT OR GRANT NUMBER(s) F19628-81-C-0081
9. PERFORMING ORGANIZATION NAME AND ADDRESS Hughes Research Laboratories 3011 Malibu Canyon Road Malibu CA 90265		10. PROGRAM ELEMENT, PROJECT, TASK AREA & WORK UNIT NUMBERS 61101F LD1613C1
11. CONTROLLING OFFICE NAME AND ADDRESS Rome Air Development Center (ESM) Hanscom AFB MA 01731		12. REPORT DATE November 1983
		13. NUMBER OF PAGES 96
14. MONITORING AGENCY NAME & ADDRESS*(if different from Controlling Office)* Same		15. SECURITY CLASS. *(of this report)* UNCLASSIFIED
		15a. DECLASSIFICATION/DOWNGRADING SCHEDULE N/A

16. DISTRIBUTION STATEMENT *(of this Report)*

Approved for public release; distribution unlimited.

17. DISTRIBUTION STATEMENT *(of the abstract entered in Block 20, if different from Report)*

Same

18. SUPPLEMENTARY NOTES

RADC Project Engineer: John J. Larkin (ESM)

This effort was funded in part by the Laboratory Directors' Fund

19. KEY WORDS *(Continue on reverse side if necessary and identify by block number)*

Electro-optic materials	Non-linear materials
Acousto-optic materials	Degenerate four-wave mixing materials
SAW device materials	

20. ABSTRACT *(Continue on reverse side if necessary and identify by block number)*

Improved materials are required for active optical devices, including electro-optic and acousto-optic modulators, switches and tunable filters, as well as for new devices based on degenerate four-wave mixing.

New materials are also needed for surface acoustic wave (SAW) applications where the lack of materials with large coupling coefficients and inherent temperature stability has limited the bandwidth of SAW devices and made

(Cont'd)

DD FORM
1 JAN 73   **1473**   EDITION OF 1 NOV 65 IS OBSOLETE

them unsuitable for many microwave applications. In addition, electro-optic and acousto-optic devices are materials limited because the materials currently available are inefficient in terms of power required and often absorb light in the regions in which operation is desired.

The primary objectives of this program include the synthesis and evaluation of new ternary chalcogenides for nonlinear and acoustical applications, and subsequently, the investigation of these materials for applications involving the electro-optic effect, degenerate four-wave mixing and surface acoustic wave technology.

The most significant development resulting from this investigation is the single crystal growth and evaluation of a new infrared-transmitting electro-optic crystal, $CdIn_2Te_4$, which we determined to have an electro-optic (EO) coefficient ($r_{41}=r_{52}$) of approximately 50 pm/V. This is an order of magnitude larger than most known IR materials, and even higher than $LiNbO_3$ (approximately 32 pm/V). We predicted a large EO coefficient for this crystal based upon the structural analog approach described in Section 2. This material transmits from 1.2 μm to beyond 16 μm; initial results indicate possible transmission to 50 μm, but the appearance of some structure in the spectral scan has not yet been resolved. The large EO coefficient significantly reduces voltage requirements and therefore allows an engineering margin for driver chips for IR EO modulators and IR tunable spectral filters.

Additional materials were sought with larger acousto-optic (AO) figures of merit and large non-linear coefficients. These materials included $AgGaTe_2$, $ZnIn_2S_4$, $ZnIn_2Se_4$, $ZnIn_2Te_4$, $ZnGa_2S_4$, $CdGa_2S_4$, $ZnGeP_2$, $AgGaS_2$, $TlVS_3$, and Tl_3VS_4. A variety of synthesis techniques were pursued, but not all of the compounds listed were successfully synthesized. Reaction to yield the ternary compound without additional phases was successful for $CdGa_2S_4$, $AgGaTe_2$, $AgGaS_2$, and $ZnGeP_2$. The two latter materials were also grown as single crystals in order to evaluate their acousto-optic and non-linear properties.

Materials characterization was carried out using x-ray powder diffraction, Read camera techniques, Laue single crystal techniques, and Hall measurements. Optical transmission was determined on selected samples. A significant effort was placed on the development of a new technique for the determination of stress optic properties of crystals: Anisotropic Transmission Ellipsometry. An initial apparatus was built but is not yet in use.

A theoretical model was developed for the electro-optic effect in crystals. This followed the development of a method for the calculation of the electronic and ionic contributions of the EO coefficient based on bonding forces in the lattice which was completed on a previous program. A first theoretical look was taken at a photo-elastic model.

TABLE OF CONTENTS

4

LIST OF ILLUSTRATIONS

SECTION 1

INTRODUCTION AND SUMMARY

A. INTRODUCTION

Improved materials are required for active optical devices, including electro-optic and acousto-optic modulators, switches and tunable filters, as well as for new devices based on degenerate four-wave mixing. Utilization of four-wave mixing techniques in practical devices could greatly increase optical system integration by expanding the possibilities of amplification, convolution, correlation, pulse compression, etc. New materials are also needed for surface acoustic wave (SAW) applications where the lack of materials with large coupling coefficients and inherent temperature stability, at least along one crystallographic orientation, has limited the bandwidth of SAW devices and made them unsuitable for many microwave applications. New materials are needed for electro-optic and acousto-optic devices because the materials currently available are inefficient in terms of power required and often absorb light in the region in which the operation is desired. At present, no materials have been identified which have sufficiently high third-order optical susceptibilities to make four-wave mixing devices.

Since electro-optical and acousto-optical devices based on currently available materials typically require much more power than can be generated by an electronic integrated circuit chip, the level of integration and hybridization is far below that desired by the Air Force. In addition, currently available materials have poor spectral characteristics in the mid and far infrared regions of the spectrum which are of great interest in current and proposed systems. The chalcogenides are predicted to have higher figures of merit and lower absorption in these spectral linearities in their optical behavior, which may make them suitable for applications in degenerate four-wave mixing. Despite its tremendous potential, four-wave mixing remains a laboratory phenomena because no suitable material has been discovered to realize its device applications. Finally, of the very few high-coupling temperature-compensated surface acoustic wave materials which have been discovered or predicted, two are ternary chalcogenides (thallium vanadium

sulfide and thallium tantalum selenide). These materials do not fit the phenomenological model used to predict temperature compensation in SAW materials, leading to the conclusion that their behavior is due to some anomaly in the chalcogenide bond in these ternary structures. Although these thallium compounds have unfavorable mechanical properties, there is reason to believe that other ternary chalcogenides may be suitable for SAW materials.

During this investigation, our plan was to synthesize and grow a series of new ternary chalcogenide compounds, evaluate them for electro-optic, nonlinear optical and acousto-optical applications, and determine the usefulness of ternary chalcogenides for applications involving the electro-optic effect, degenerate four-wave mixing, and surface acoustic-wave technology. Materials grown were predicted both on the basis of crystal chemical considerations and from a concurrent theoretical exploration of those conditions which will maximize the properties desired.

B. SUMMARY

The most significant development resulting from this investigation is the single crystal growth and evaluation of a new infrared-transmitting electro-optic crystal, $CdIn_2Te_4$, which we determined to have an electro-optic (EO) coefficient ($r_{41}=r_{52}$) of approximately 50 pm/V. This is an order of magnitude larger than most known IR materials, and even higher than $LiNbO_3$ (approximately 32 pm/V). We predicted a large EO coefficient for this crystal based upon the structural analog approach described in Section 2. This material transmits from 1.2 μm to beyond 16 μm; initial results indicate possible transmission to 50 μm, but the appearance of some structure in the spectral scan has not yet been resolved. The large EO coefficient significantly reduces voltage requirements and therefore allows an engineering margin for driver chips for far infrared EO modulators and IR tunable spectral filters. This work represents the prime effort made during the course of this investigation. Measurement of the other electro-optic coefficients revealed comparatively low values (not unlike $LiNbO_3$ r_c 5.5 pm/V; r_{13} = 0.15 pm/V.

8

Additional materials were investigated in search of new materials with larger acousto-optic (AO) figures of merit and large non-linear coefficients. These materials included $AgGaTe_2$, $ZnIn_2S_4$, $ZnIn_2Se_4$, $ZnIn_2Te_4$, $ZnGa_2S_4$, $CdGa_2S_4$, $ZnGeP_2$, $AgGaS_2$, $TlVS_3$, and Tl_3VS_4. A variety of synthesis techniques were pursued as described in Section 3B, "Synthesis of New Ternary Chalcogenide Compounds". However, not all of the compounds listed were successfully synthesized. Reaction to yield the ternary compound without additional phases was successful for $CdGa_2S_4$, $AgGaTe_2$, $AgGaS_2$, and $ZnGeP_2$. The two latter materials were also grown as single crystals in order to evaluate their acousto-optic and non-linear properties. The remainder of the materials invariably contained intermediate binary phases or yielded other than the desired stoichiometry.

Materials characterization was carried out using x-ray powder diffraction initially to identify the material. Read camera techniques were used when the powder diffraction data was not sufficiently sensitive and left some unanswered questions, especially concerning the presence of additional phases. Crystals were characterized by Hall measurements, where appropriate, to determine resistivity, mobility, and type. Bulk resistivity measurements were also made on large crystal samples when available. In addition, optical transmission in the visible and infrared spectral regions was determined. Differential thermal analysis (DTA) was used to determine melting characteristics as well as the existence of other phase transitions for selected compounds. DTA was also used to determine reaction phenomena. A significant effort was placed on the development of a new technique for the determination of stress optic properties of crystals: Anisotropic Transmission Ellipsometry. This is discussed in detail in Section 6, "Optical Evaluation of Crystals". Our initial apparatus required some modifications which were not completed until the end of this project.

The theoretical aspects of anisotopic transmission ellipsometry are detailed in this report. A theoretical model was developed for the electro-optic effect in crystals. This followed the development of a method for the calculation of the electronic and ionic contributions of the EO coefficient based on bonding forces in the lattice which was completed on a previous program. A first cut was taken at a photo-elastic model (Section 5).

SECTION 2

APPROACH

A OBJECTIVE

The primary objectives of this program include the synthesis and
evaluation of new ternary compounds, especially chalcogenides, for nonlinear
and acoustical applications; and subsequently, the investigation of these
materials for applications involving the electro-optic effect, the acousto-
optic effect, degenerate four-wave mixing, and surface acoustic wave
technology.

B. APPROACH SUMMARY

The approach to the selection of new electro-optic and acousto-optic
materials to be evaluated for the many applications noted is discussed in
detail in Section 2D. A brief summary is presented here. Our approach is
based on selection and prediction of materials having similar structures to
known materials which have demonstrated optimum properties in the desired area,
i.e., electro-optic, acousto-optic, nonlinear, etc. The main structural
characteristics used are the ionic coordination and the point group. Analog
families of compounds are so selected and then expanded by ionic substitution —
which holds structurally within certain ionic size limits. A valuable aspect
to this type of program is the ability to evaluate polycrystalline samples
since the growth of single crystals can take a long period of time and limit
the number of crystals examined. This approach works well using the low
frequency dielectric constant as a guide for electro-optic properties — and may
carry over as well for acousto-optic and nonlinear properties. A portion of
this effort is devoted to seeking evaluation techniques for polycrystalline
materials related to the acousto-optic coefficient. We investigated
optical evaluation techniques typically used for single crystals which might
offer a potential mode for optical evaluation of polycrystalline samples.
Theoretical considerations of the relationships of measurable properties on
polycrystalline samples to the optical properties of interest was pursued by
Professor Amnon Yariv (Caltech), as a consultant to Hughes Research
Laboratories and this program.

11

C. BACKGROUND

Approximately four years ago, personnel at Hughes Research Laboratories (HRL) reviewed the requirements for an infrared (IR) transmitting, spectrally tunable filter for the HALO technology program. We concluded that both the total power consumption and the drive-power density would be excessive if an acousto-optic (AO) filter were used. This led us toward the invention of an electro-optic (EO) analog to the AO filter. Such a filter would require orders of magnitude less drive power. Progress on the reduction to practice of this invention has been excellent, but development work is not without technical risks. The test-sample-acquisition and materials-development tasks we completed in pursuit of the filter provided us with a data base of EO crystals (mostly with the chalcopyrite structure) from which $AgGaS_2$ was selected for the HALO program. Subsequently, a materials program aimed at increasing the scope of IR-transmitting EO materials was sponsored by DARPA[1] to develop new materials with the potential of having an EO coefficient many times larger than the chalcopyrites, and hence, of providing an engineering margin in filter design with respect to the voltage requirements of the drive chip. This program succeeded in identifying two new materials, $CdIn_2Te_4$ and $AgGaTe_2$, that may have an EO coefficient at least an order of magnitude greater than that of $AsGaS_2$ and would thereby reduce required maximum drive voltages to no greater than 100 V. In a coordinated effort between HRL and the California Institute of Technology (Caltech), a review of fundamental EO concepts by Professor Yariv (Applied Physics Dept., Caltech) has led to the extension of current theory and to a method of calculating the EO coefficient using structural data.

D. SELECTION OF NEW MATERIALS

A review of the classes from which EO crystals can be selected (Figure 1) shows that some of these classes are also applicable to collinear AO effects. In addition, many of the properties that lead to a larger EO coefficient and figure of merit (e.g., large refractive index and octahedral coordination, as discussed below) also lead to materials with an improved AO figure of merit, as well as larger nonlinear effects. DoD interest in AO devices for optical information processing, optical switches, modulators, correlators, and

TYPE	POINT GROUP
CUBIC	23, M3, 432, $\overline{4}$3M, M3M
HEXAGONAL	6, $\overline{6}$, 6/M, 622, 6MM, $\overline{6}$M2, 6/MMM
TRIGONAL	3, $\overline{3}$, 32, 3M, 3M
TETRAGONAL	4, $\overline{4}$, 4/M, 422, 4MM, $\overline{4}$2M, 4/MMM
ORTHORHOMBIC	222, MM2, MMM
MONOCLINIC	2, M, 2/M
TRICLINIC	1, $\overline{1}$

◯ LONGITUDINAL   ◇ ACOUSTO-OPTIC (COLINEAR)

□ TRANSVERSE

Figure 1.   Crystal structures useful for AO/EO selection.

13

scanners led us to evaluate an approach similar to the analog selection used for new EO materials, as described below, and to look for new, improved AO materials.

The AO figure of merit (M_2) can be expressed as

$$M_2 = \frac{n^6 p^2}{\rho V^3} \quad ,$$

where n is the index of refraction, p is the photoelastic constant, ρ is the density, and V is the acoustic velocity. The quantities n, p, and V are related to tensor quantities and therefore can vary with crystal orientation. The photoelastic constant, which is the basis for the AO effect, is not limited to specific symmetry classes, but the collinear AO effect, as indicated in Figure 1, is symmetry dependent. Other AO figures of merit (M_1, M_3) described in the literature[2][3] may be more or less applicable to particular device designs. However, all the AO figures of merit are maximized in materials having

- High refractive index
- High photoelastic component
- Low density
- Low sound velocity.

An additional property, one which is normally not incorporated in figures of merit but is of vital importance to device design, is the intrinsic acoustic loss (α) of a material. Transparent liquids, for example, typically have high acoustic attenuation above 50 MHz, although they may have a high figure of merit. The acoustic attenuation must be determined for potential, new AO materials.

Our approach to finding new materials is based on selecting structural analogs to the best observed EO and AO materials in the visible spectrum range (e.g., $LiNbO_3$, $LiTaO_3$, and $PbMoO_4$). We concentrated primarily on IR and mm-wave transmitting compounds.

Criteria for materials selection, including crystal class, structural similarities, and the proportional scaling of radius ratios of the components, make up general guidelines for new materials choices. Often, where crystallographic data is available, the radius scale-up leads to different

crystal structures and classes that do not fit the requirements for the EO or AO effects. Use of chemical periodicity in all cases indicates the possibility of predicting improvement within a structural type, but the accuracy of the prediction is uncertain, and the magnitude unknown and often small.

A search for new materials through compilations of compound semiconductor and semi-insulator crystals reveals numerous possibilities, such as those shown in Figure 2. This search reveals considerable controversy concerning crystal class as well as several unknown properties of these materials.

Applying the principles of crystal chemistry to a structural analog of lithium niobate within an allowed crystal class, we predicted similarly large EO coefficients in a chalcogenide material, $CdIn_2Te_4$. A detailed analysis of the $LiNbO_3$ structure (Figure 3) shows that it consists of a planar sheet structure of anions (oxygen) in approximately hexagonal close packing. This results in distorted, partially occupied octahedral sites (essentially, a defect structure). These sites are one-third occupied by niobium, and one-third by lithium; the remainder are vacant. The sequence of distorted octahedra along the c-axis with Nb at the origin is Nb-V-Li-Nb-Li, where V is a vacancy.

A plot of the vertical position of Nb (in an octahedral site) versus potential energy (Figure 4) shows curves for temperature above and below the Curie point (T_C). The existence of curve 2 (with $T \approx T_C$) indicates a large ionic contribution to the polarizability, yielding a large EO coefficient, which, for $LiNbO_3$, is 32×10^{-12} m/V. The AO figure of merit for $LiNbO_3$ is shown with other materials in Table 1. One obstacle in seeking structural analogs among IR-transmitting chalcogenides appeared to be the typical tetrahedral coordination of these semiconducting materials (e.g., zincblende and chalcopyrite structures). The importance of the octahedral coordination in the selection of AO materials has been indicated by Pinnow.[4] In a previous investigation,[5] we uncovered a group of materials of the general formula, $A^{II} B_2^{III} C_4^{VI}$, that are closely analogous to $LiNbO_3$ and thereby show considerable promise of having high EO coefficients. These materials have been described as crystallizing in the crystal classes 3m (same as $LiNbO_3$), $\bar{4}$, and $\bar{4}$ 2m (same as chalcopyrites); all of these are usable for EO and/or AO devices.

The 3m point group, of which $ZnIn_2S_4$ is a member (Figures 5 and 6), has a unit cell consisting of 12 closely packed sulfur layers. Octahedral sites contain one-half the total number of In atoms; the Zn and the other half of the

15

POINT GROUP	CRYSTALS
6	$La_3 Cu Si S_7$, $Ln_3 Ag Ge S_7$ (Ln = LANTHANIDE) $Ba C S_3$, $Sr C S_3$
622	$Nb Ge_2$, $Ta Ge_2$
4	$A B_2 X_4$ (X CHALCOGENIDE) $Cd Ga_2 S_4$, $Zn Ga_2 Se_4$, $Zn Ga_2 Te_4$ $Cd In_2 Te_4$
42 m	$Cd In_2 Se_4$ $Cu_2 Cd Ge Se_4$ CHALCOPYRITES: $Cu Tl S_2$, $Cu Tl Se_2$ $Ag In_5 Se_8$
2	$Ln Ag S_2$ (Ln Sm, Gd, Tb, Dy, Y, Ho, Er, Tm)
3 m	$Zn In_2 S_4$, $Cd Ga_2 Se_4$ PROUSTITE FAMILY: $Ag_3 As S_3$, $Tl_3 As Se_3$
mm2	$A_2 B X_4$ (X = CHALCOGENIDE): $Ba_2 Sn S_4$, $Z_n Al_2 S_4$ $Y Sc S_3$, $La Yb S_3$ $Ge S_2$, $Ge Se_2$ (?) Ti Ge $Cu_2 Cd Ge S_4$

Figure 2. Examples of possible new EO/AO materials.

6364-10A

○ Li

○ Nb

○ O

C_{3v}^{5} (3 m)
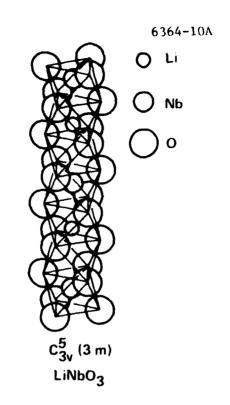
LiNbO₃

Figure 3. LiNbO₃ structure.

LiNbO₃

Nb

O

6364-20

VERTICAL POSITION OF Nb

POTENTIAL ENERGY

③

② T ≈ T_C

①

①

②

③
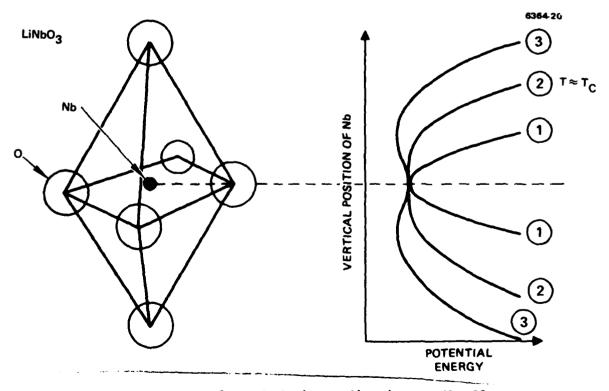
Figure 4. Importance of octahedral coordination to EO effect.

17

Table 1. Comparison of AO Materials.

Material (Point Group)	Useful Optical Transmission, µm	Refractive Index, 2 µm	Density (ρ), g/cm^3	Maximum AO Figure of Merit (M_2)
$\alpha - SiO_2$	0.2 to 2	1.52	2.65	5
$CaMoO_4$ (4/m)	0.4 to 4.5	1.95	4.26	118
$PbMoO_4$	0.4 to 5.5	——	6.95	23.7
$LiNbO_3$ (3m)	0.4 to 4.5	2.2	4.64	217
Tl_3AsSe_3	1.27 to 18	3.3	7.83	>500

6364-12

PROPERTY	$LiNbO_3$	$ZnIn_2S_4$	$Cd\,In_2\,Te_2$
CRYSTAL CLASS	3 m	3 m	$\bar{4}$
STRUCTURE CHARACTER	DEFECT	DEFECT	DEFECT
ANIONS	LAYER CLOSE PACKING (OXYGEN)	LAYER CLOSE PACKING (SULFUR)	LAYER CLOSE PACKING (TELLURIUM)
COORDINATION	DISTORTED OCTAHEDRAL	MIXED OCTAHEDRAL TETRAHEDRAL	MIXED (INVERSE) OCTAHEDRAL TETRAHEDRAL
SITE OCCUPANCY	1/3 Nb 1/3 Li 1/3 VACANCY	OCTAHEDRAL $\{$ 1/2 In$_{total}$ TETRAHEDRAL $\{$ 1/2 In$_{total}$ Zn$_{total}$ 2 VACANT METAL SITES "DEFECT CHALCOPYRITE"	1/2 In$_{total}$ Cd$_{total}$ 1/2 In$_{total}$
E-O COEFFICIENT, r_{ij}	32×10^{-12} m/V	?	$\sim 50 \times 10^{-12}$ m/V

Figure 5. New EO/AO materials — analog selection.

18

6364-10

C_{3v}^5 (3 m)
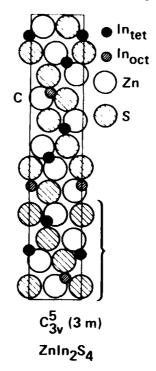
$ZnIn_2S_4$

Figure 6. Structure of $ZnIn_2S_4$.

In atoms are in tetrahedral sites. An inverse structure has also been described in which the divalent and one-half of the trivalent atoms are in octahedral sites and one-half of the trivalent atoms are in tetrahedral sites, which leaves a fraction of vacancies in each type of site. The inverse structure has been described for X In_2S_4, where X is Mg, Fe, Co, Ni, $CdGa_2S_4$, $HgIn_2S_4$, or $CdIn_2Te_4$. Existing theories of the EO effect in crystals indicated that the EO coefficients of these materials should be significantly higher than those of the chalcopyrites.

There is little published data concerning the properties of these materials. A shift in conductivity of more than five orders of magnitude has been reported for $CdIn_2Se_4$ annealed in Se vapor. The transmission of $CdIn_2Te_4$ has been reported in the range of 1 to 37 μm. Carrier mobilities in these materials are usually not greater than tens of $cm^2V^{-1}sec^{-1}$, which is typical of ternary chalcogenides. $CdIn_2Te_4$ is reported to have the symmetry of $\overline{4}$ crystal class. Because of the open crystal structure, which has vacancies when derived from the standard zincblende unit, they are considered "defect" structures. A structural classification of $A^{II} B_2^{III} C_4^{VI}$ compounds is illustrated in Figure 7 (Ref. 6).

19
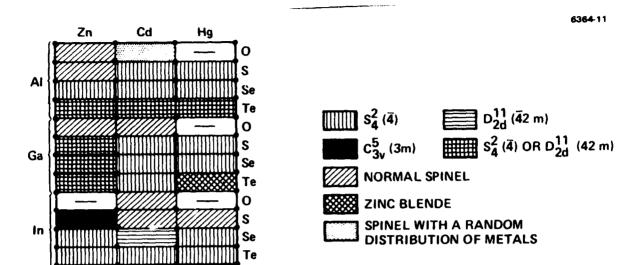
Figure 7.   Structures of $A^{II} B_2^{III} C_4^{VI}$ compounds (Ref 6).

A new theoretical approach for calculating the EO coefficient of these compounds has been worked out by A. Yariv and C. Shih[7] at Caltech. This approach utilizes the structural crystallographic components, e.g., bond lengths and angles, along with measured values of the low frequency dielectric constant, to predict values for the EO coefficient. The results show very close agreement to measured values for both binary and ternary compounds. Calculations for $CdIn_2 Te_4$ and $ZnIn_2 S_4$ indicate that they may have huge EO coefficients.

Measurements of the low-frequency dielectric constant, which was used as a guide to high EO coefficient, have been made on a DARPA-sponsored program for some of these materials (Table 2) which we successfully synthesized. Two materials, $CdIn_2 Te_4$ and $AgGaTe_2$, were selected because of their high values of low-frequency dielectric constant for eventual single crystal growth and evaluation of the EO coefficient, as well as AO and nonlinear properties.

The pertinent properties relating to a large AO figure of merit include, as mentioned above, a large index of refraction, a large photoelastic component, low density, and low acoustic velocity. The index of refraction can be related to density (ρ) and chemical composition, as shown by Gladstone and Dale:[8]

$$\frac{n-1}{\rho} = K = \sum P_i k_i \quad,$$

Table 2. Dielectric Constants at Indicated Frequencies for Some
Binary Ternary Chalcogenides (Ref. 5).

Compound	Dielectric Constant	Frequency, kHz
GeS_2	10.7	10
$GeSe_2$	5.32	6
	5.31	50
	5.30	100
	5.26	400
$AgGaS_2$	13.7	10
$AgGaTe_2$	200	5
	270	1000
$ZnSiAs_2$	34.78	6
	34.65	10
	33.64	100
	32.91	400
$ZnGa_2S_4$	62.1	6
	40.9	10
	35.8	20
	21.3	50
	18.1	100
	13.5	400
$CuInSe_2$	36.81	6
	36.15	10
	35.74	100
	35.71	400
Cu_2GeS_3	49	10
$Cu_2CdGeTe_4$	60.3	10
$CdIn_2Te_4$	264.5	10

where k is known as the specific refractive energy of the compound, and the k_i are the specific refractive energies of the components whose weight percentages are p_i. The relationship of index of refraction (n) to energy gap, as shown for oxides in Figure 8, has been explained by Wemple and DiDomenico.[9][10] Thus, one can realize that ternary sulfides comprise a group of typically high-index materials and conclude that the maximum index of refraction for an AO medium is limited by the selection of the shortest wavelength for which optical transmission is desired.

Pinnow[4] has shown the relationship of acoustic velocity to the mean atomic weight, M (defined as the total molecular weight divided by the number of atoms per molecule), for oxides, alkali halides, and some semiconductors (Figures 9, 10, and 11). Typically, the V/p ratio decreases with increasing M.

A compilation[4] of measured photoelastic components for oxides, alkali halides, and some III-V and chalcogenide compounds indicates variations over a fairly narrow range. The average photoelastic component, in both ionic and covalent limits, can be attributed to two effects:

- Increase in n due to increase in packing density

- Change in n due to change in polarizability under compression.

The latter effect is one shown (in the EO coefficient) to have large effects when the compound contains heavier (more polarizable) atoms (electronic polarizability) or when the structure is more "open," allowing larger ionic polarizability. In our analysis of the EO coefficient, we predicted that ionic polarizability and EO coefficient would tend to be larger in compounds having octahedral coordination than in those having tetrahedral coordination, although the effect of large atoms cannot be completely ignored. Indeed, this appears (from examples such as $PbMoO_4$, $SrTiO_3$, and $LiNbO_3$) to hold as well for large photoelastic effects and, hence, large AO figures of merit. The figure of merit (M_2) is 23.7 ($0.4 < \lambda < 5.5$) for $PbMoO_4$ and 21.7 ($0.5 < \lambda < 4.5$) for $LiNbO_3$. In summary, although optimum trade-offs must be sought for maximizing the AO figure of merit, the materials properties desired can be found among the same classes of ternary compounds that we have selected for investigation
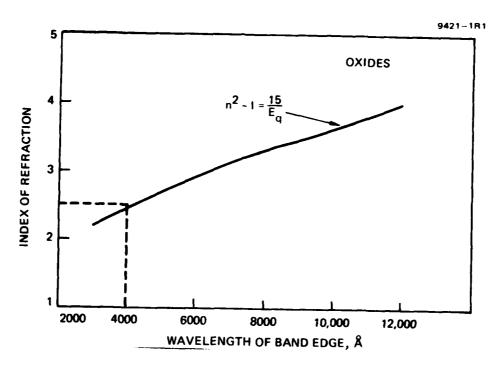
Figure 8. The index of refraction for oxide material is related to its energy gap E_g by the equation shown, where units for E_g are electron-volts. The expression has been plotted as index versus wavelength corresponding to band edge to demonstrate that maximum index is determined by the shortest wavelength for which optical transmission is desired.

seeking higher EO coefficients. Recent work[11] has indicated that Tl_3AsSe_3 (a proustite analog) has a figure of merit $(1.27 < \lambda < 18 \ \mu m)$ greater than 500. The AO figure of merit for several compounds is shown in Table 1.

We investigated the measurement of the elastic constants of materials by a new technique, anisotropic transmission ellipsometry, which is discussed in detail below.

Based on the large non-linear coefficient for some ternary compounds of the type $A^{II} B^{IV} C_2^V$, e.g., $CdGeAs_2$, we studied synthesizing some of these compounds; the most successful of these was $ZnGeP_2$. Following this approach for selecting new SAW device and acousto-optic materials, we noted several ternary compounds of thallium, i.e., Tl_3AsSe_3, $TlVS_3$, which have large acousto-optic figures of merit. Thallium is particularly interesting because of its capability to exist in compounds in both monovalent and
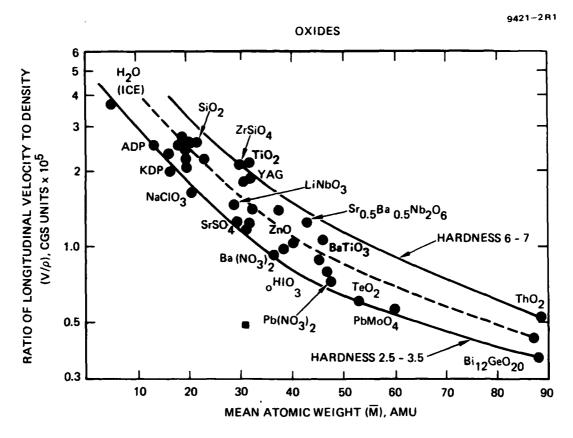
OXIDES

Figure 9. Velocity-density ratio versus mean atomic weight for mineral
oxides. The upper solid curve is applicable to compounds with
Mohs' hardness in range of 6-7; the intermediate dashed curve is
for compounds with hardness of 4-5; and the lower solid curve is
for compounds with hardness of 2.5-3.5.

trivalent states, readily substituting for both Group I (Ag, Cu) and Group III
(Al, Ga, In) atoms. In addition, the thallium atom is relatively large; such
compounds can be expected to show large electronic and ionic polarizabilities.
As yet (to our knowledge), no one has succeeded in synthesizing a "ternary"
compound containing Tl^{+1} and Tl^{+3} (essentially thallium in two different
lattice cation sites). The compounds of thallium with Group VB atoms,
especially vanadium, are interesting as well because of the variable valence
possibilities for vanadium.

24
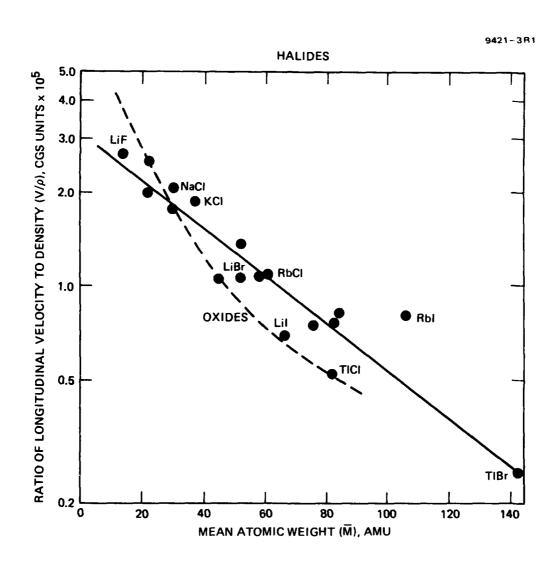
Figure 10. Velocity-density ratio versus mean atomic weight for halides.
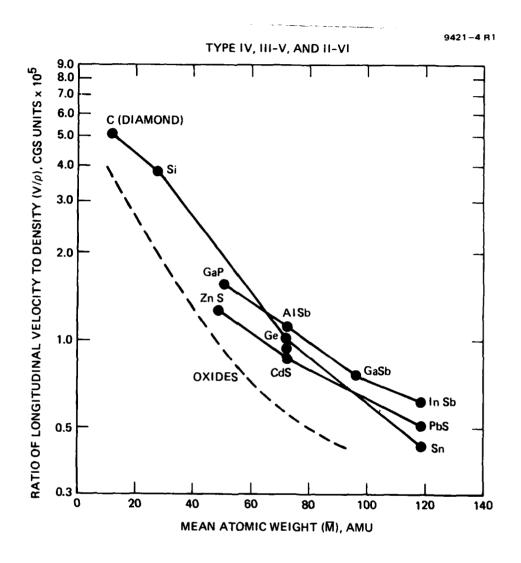
Figure 11. Velocity-density ratio versus mean atomic weight for group IV, III-V, and II-VI compounds.

SECTION 3

MATERIALS SYNTHESIS AND CHARACTERIZATION

A. $CdIn_2Te_4$

1.   Material Synthesis

Our initial experiments were primarily concerned with growth of single crystals of $CdIn_2Te_4$ to demonstrate the feasibility of our approach. This compound crystallizes in the point group 4 (Ref. 6) and is applicable for both electro-optic (longitudinal or transverse) and acousto-optic (collinear) applications. This compound was selected from several which we previously identified (Ref. 5) as having large low-frequency dielectric constants and, therefore, the potential for large electro-optic coefficients (Ref. 7).

The pseudobinary phase diagram for the system $CdTe-In_2Te_3$ is shown in Figure 12 (Ref. 12). The dotted line represents modifications made by A. Borshchevsky (Ref. 13), and indicates that the compound $CdIn_2Te_4$ melts incongruently at 785°C. Our approach to single crystal growth utilizes the Bridgman technique, using an off-stoichiometric composition which lies in the region between 702°C and 785°C where solid $CdIn_2Te_4$ (designated β in Figure 12) is in equilibrium with liquid (ℓ). This may be considered growth from solution — a constituent solution rich in In_2Te_3. Nucleation of a single crystal is initiated by using a conically-shaped fused silica ampoule which is evacuated and sealed after loading. Invariably, the tip has been single; but all runs to date have grown polycrystalline as the width of the ingot increases. The top of the ingot (Figure 13) reveals the solidified "solvent" from off-stoichiometric composition. Several large (>5 mm dimensions) single crystals were found in some runs. The x-ray diffraction pattern for $CdIn_2Te_4$ was obtained and is shown in Figure 14.

Although the entire ingot was not usually single, a crystal measuring approximatey 5 x 5 x 8 mm was obtained from a starting composition of 63% In_2Te_3, 37% CdTe. The growth rate was approximately 1 mm/day.

This crystal was oriented by X-ray Laue techniques, cut and polished for a variety of measurements including r_{41}, the electro-optic coefficient.

A brief study was made to determine if one of the standard semiconductor etchants would reveal grain boundaries in $CdIn_2Te_4$. Initially, we tried to sandblast the ingot, a technique which has been very successful in revealing

27
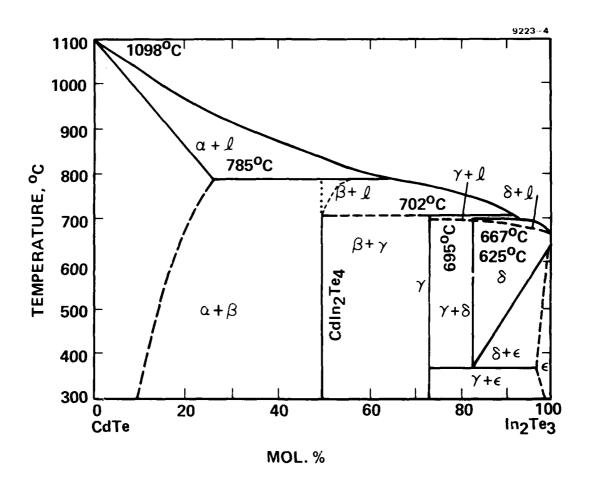
Figure 12. Phase equilibrium diagram for CdTe-In$_2$Te$_3$.

28
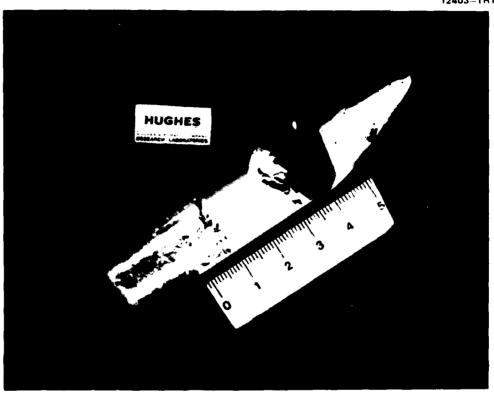
Figure 13. Ingot of $CdIn_2Te_4$.

grain boundaries in CdTe. This did not work for $CdIn_2Te_4$. All etchants used also failed to reveal grain boundaries. Bromine:methanol formed an amorphous skin on the ingot. Finally, we found that a light polish was the most effective way of revealing grain boundaries. Although IR microscopy can be used, samples require slicing to thicknesses which limit further characterization.

2. Characterization

The resistivity of the $CdIn_2Te_4$ crystal was measured to be 1.7×10^6 Ω-cm at room temperature using standard 4-point probe techniques. A transmission
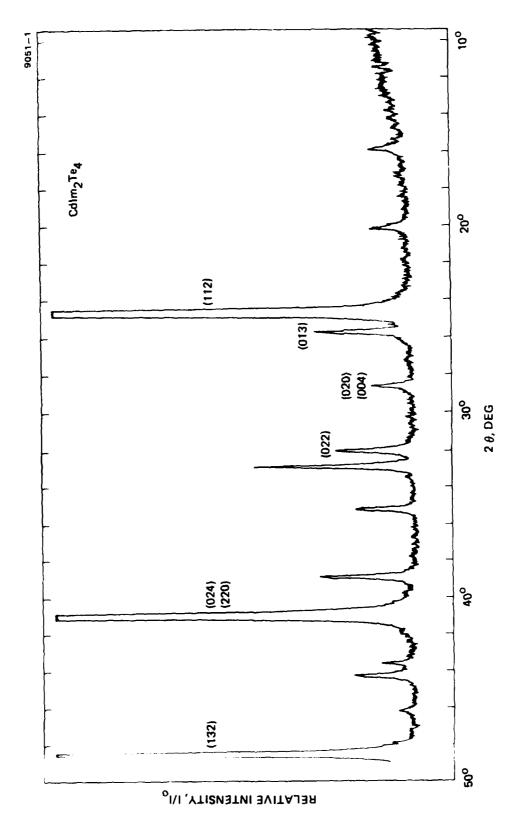
Figure 14. X-ray; diffraction pattern of $CdIn_2Te_4$.

30

spectrum (Figure 15) in the range of 2.5 to 16 µm was obtained using the Bomem Fourier Transform Spectrophotometer. The curve is very flat, indicating the absence of free carrier absorption. However, the apparent transmittance (approximately 70%) value is not absolute; the instrument requires additional calibration because of high index of refraction of the $CdIn_2Te_4$ sample. An independent measurement of the refractive index using optical thickness and the channeling effect as described below yielded an average value in the range of 2.5 to 3 µm of n = 2.95. This would correspond to a transmittance of approximately 60%. The dispersion was determined to be small. The birefringence was measured to be 0.0135 at 3 µm and 0.0122 at approximately 10 µm.

The near infrared spectrum of $CdIn_2Te_4$ was measured using a Carey Spectrophotometer. We determined the short wave cutoff to be 1.2 µm. The transmission spectrum in the range of 1.0 to 16 µm is shown in Figure 15. The dotted portion was calculated from optical density data from the Carey.

11601-1R1
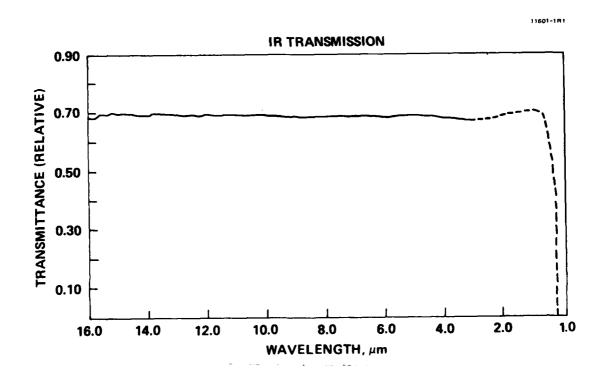
Figure 15.   Near and Far IR transmission spectrum of $CdIn_2Te_4$.

a.   Channel Spectra

The determination of the index of refraction, n, of a material is
typically accomplished by measurement of the transmission spectrum of a sample
and calculation of reflectance and n using the well known equation:

$$R = \frac{1 - T}{1 + T} \quad , \quad \text{and}$$

$$n = \frac{1 + \sqrt{R}}{1 - \sqrt{R}} \quad ,$$

where T and R are the transmission and reflection of the sample, respectively.
This discussion assumes no sample absorption. An accurate transmission value
is difficult to obtain because the increase in optical path length introduced
by the sample tends to defocus the radiation at the detector. The phenomenon
of channel spectra is also a nuisance in this measurement. The effect occurs
in moderately and highly reflective samples whose surfaces are polished and
parallel to avoid surface scatter and to obtain a definite sample thickness.
In these samples, an interference occurs between the "transmitted" beam and
that portion of the incident radiation which is internally reflected 2(or 4 or
6...) times. This interface occurs as a sinusoidal modulation of the
spectrum.

The channeling effect can be used, however, to determine the optical
thickness, nl, of a sample. Further, the channeling effect is conveniently
measured in the interferogram of a Fourier transform spectrometer where a
secondary peak in the data occurs at a mirror translation corresponding to the
same optical path as the optical thickness of the sample. Since the mirror
spacing is very accurately measured in the interferometer, the optical
thickness of a "channeling" sample is easily determined.

Thus, this phenomenon, which is normally considered to be detrimental, is actually superior to transmission measurement to determine the index of refraction of a sample, in that the technique is not sensitive to the defocusing effects of an optically thick sample in a focused beam.

b.   Hall Measurements

Hall samples were prepared and measured in our computerized Hall apparatus. The results printed out by the computer are shown in Figure 16. The samples were run at room temperature and two samples were in close agreement. The results are quite accurate, but the error ratios (0.957, 0.870) show some minor problems with contacts (truly ohmic contacts yield an error ratio of unity). Resistivity on some samples determined from the Hall measurement was ~1.5 x 10^3 Ω-cm, which significantly differed from the bulk crystal measurement; i.e., 1.7 x 10^6 Ω-cm. Initially, we assumed that the Hall measurements were correct and that the bulk measurement possibly reflects non-ohmic contacts—essentially, a measurement of bulk and contact resistance. These results were subsequently checked by additional Hall evaluations with sample etching between measurements to assure that the Hall measurement was not assessing sample surface conductivity.

Hall measurements were repeated on a sample of $CdIn_2Te_4$, primarily to determine a final value for the resistivity. In addition, four-point probe measurements were made. Final results showed that polished samples have a resistivity $\approx 10^3$ Ω-cm. When these samples are etched in a bromine methanol solution, the resistivity measures approximately 10^6 Ω-cm. We believe that surface damage from polishing creates a low ρ (conducting) surface, which is subsequently removed by etching.

```
****************************************************************
*                                                              *
*-------------------- Cd:In:Te-1 C ORIENTED. ----------------*
*                                                              *
*  H A R M 6 . 0 1                    13:55:03  02-MAR-82   *
*                                                              *
*          10V 2 TERM MAX.NO SLOTS.In CONTACTS.              *
*                                                              *
****************************************************************
2-Terminal voltages at I=2.00E-05 amps
V53=  6.958       Err-Ratio(I)= 0.957
V42=  6.860       Err-Ratio(I)= 0.870

Sample. Cd:In:Te-1 C ORIENTED.                    13:57:03  02-MAR-82
Sample. I=2.00E-05, Thickness=0.5291    mm; rds  delay= 0.500 secs; #rdss= 1
              RESISTIVITY   MEASUREMENTS
R54/23=  7678         Err-Ratio(I)= 0.982  Err-Ratio(S)= 0.975  ~Volts= 1.54E-01
R43/52=  4960.        Err-Ratio(I)= 0.982  Err-Ratio(S)= 0.968  ~Volts= 9.92E-02

Rho sa= 2.8176E+04  Rho(ohm-cm)=  1491      F=0.9838  R-ratio= 1.548

              HALL   MEASUREMENTS
V(H)-volts  Erat(I)  Symm(H)  Offset(H)  Zro-drft  Zro-curv  Field(gauss)
 3.651E-04   0.812   0.958    -0.010      0.091     0.0575     10030.6

    Mu         Mu*B       R(H)        N/cc       N/sqcm
  6.460      0.0006    9.631E+03   6.481E+14   3.429E+13


The maximum weighted error was:   0.094
```

Figure 16. Computer print-out for Hall measurements.

c. **Measurement of Electro-Optic Coefficient**

In preparation for measuring the electro-optic coefficient, r_{41} ($=r_{52}$), of $CdIn_2Te_4$, the <100> faces of an x-cut sample were coated with indium-tin oxide (ITO) electrodes. Thin layers (150 Å) of ITO were deposited directly on the sample at a temperature of 200°C. Layers such as these exhibit relatively low resistance as well as good transmission from the near IR out to beyond 10 μm.

After wiring the sample to the driver circuitry, we found that only about 50 V could be applied to the crystal before the ~18 mA current limit of the driver was exceeded. For the 4 x 6 x 1.13 mm sample, this value corresponds to an apparent resistivity of $\rho = 6 \times 10^3$ Ω-cm.

34

Since contact effects between metals and semiconductors can often cause erroneous resistance readings, the sample's I-V characteristic was examined and is shown in Figure 17(a). In response to a triangular voltage wave (top trace), the sample drew a highly nonlinear current (bottom trace). The current is seen to vary roughly exponentially with voltage, implying that a rectifying contact has been formed between the ITO and the $CdIn_2Te_4$. A similar I-V characteristic was observed when another sample with silver paint electrodes was examined (see Figure 17 (b)).

The different resistivity values observed above are at least partially due to contact problems and are not characteristic of the bulk material. In order to avoid these effects in our electro-optic measurements, subsequent samples were prepared with an insulating layer of SiO_2 between the ITO and the $CdIn_2Te_4$ surface for measurement of r_{41}.
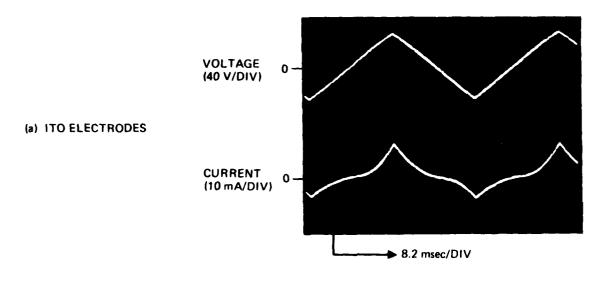
A preliminary value of $r_{41} \approx 50 \times 10^{-12}$ m/V was determined using a simple ratio measurement technique. At first, serious discrepancies between theory and experiment, made the above value suspect; the disagreement was determined to be caused by twinning in the samples tested.

For these tests, x-cut samples 1.10 to 1.13 mm thick were coated with 2000 to 5000-Å layers of SiO_2, followed by indium-tin-oxide (ITO) electrode layers approximately 400 Å thick. The resistivities of the ITO layers were approximately 200 Ω/square. The SiO_2 layers were required to prevent the injection effects described in the previous quarterly report. Complete blocking was apparently achieved since essentially no current was drawn by the samples for applied voltages up to 100 V.

The measurement technique involves applying an ac field to the sample along the x direction and measuring the ratio of the modulated component of the transmitted light to the unmodulated component. The sample was placed between polarizers oriented as shown in Figure 18. For this arrangement, the ratio of the ac signal to the (chopped) dc signal is

$$R \equiv \frac{4\bar{n}^3 \, r_{41} E}{\Delta n} \, \sin^2 \left(\frac{\Gamma}{2}\right) \quad , \tag{10}$$

VOLTAGE
(40 V/DIV) 0 —

(a) ITO ELECTRODES

CURRENT
(10 mA/DIV) 0 —

8.2 msec/DIV

VOLTAGE
(40 V/DIV) 0 —

(b) SILVERPAINT ELECTRODES

CURRENT
(10 mA/DIV) 0 —

8.2 msec/DIV
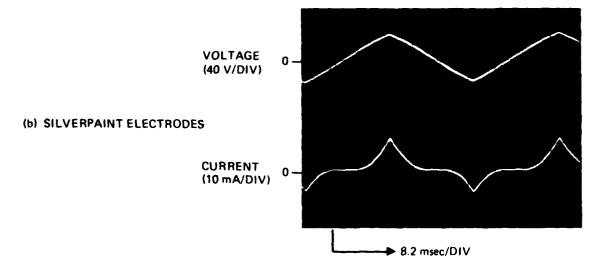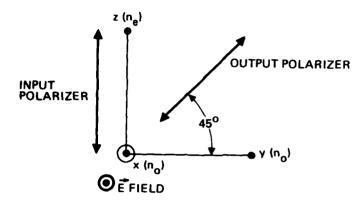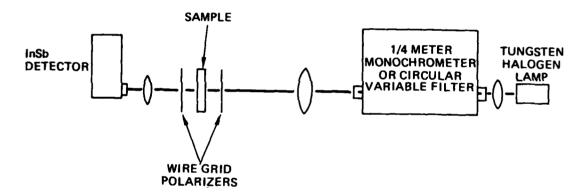
Figure 17.   I-V characteristic of $CdIn_2Te_4$:
        (a)   ITO electrodes
        (b)   silver paint electrodes.

SAMPLE AND POLARIZER ORIENTATION

EXPERIMENTAL APPARATUS

ELECTRONICS
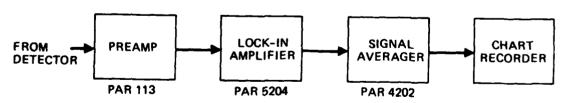
Figure 18.   Apparatus for measurement of r_{41}.

where

$$\Gamma = \frac{2\pi L \Delta \bar{n}}{\lambda} \quad . \tag{2}$$

Here $\bar{n} = 1/2 \ (n_o + n_e)$, E is the electric field, Δn is the birefringence, L is the sample thickness, and λ is the wavelength. We have also assumed detection of both components by a lock-in amplifier. Solving Equation (1) for r_{41} gives

$$r_{41} = \frac{\Delta n R}{4 \bar{n}^3 E \ \sin^2 \frac{\Gamma}{2}} \quad . \tag{3}$$

According to Equation (1), the largest values for R are obtained when the retardation (Γ) is an odd multiple of π. Thus, it is best to choose a wavelength for the measurement that produces this maximum. Making the measurement at a maximum has the added benefit that the sample thickness (L) need not be known.

A schematic of the experimental apparatus is shown in Figure 18. A tungsten halogen lamp is used as a light source, with either a 1/4 meter monochromator or a circular variable filter acting as a wavelength selective device. The light is directed through the sample in an F/4 light cone and detected with an InSb detector. Signal averaging is provided by a PAR 5204 lock-in.
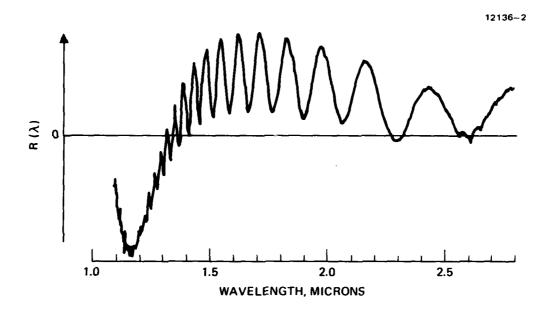
In order to find the wavelengths at which R is a maximum, two wavelength scans are performed in series. In the first scan, the modulation component of the signal is determined, with the lock-in output stored in one memory channel of a PAR 4202 signal averager. On the second scan, the dc (chopped) component of the signal is measured and stored in a second memory channel. The PAR 4202 is then used to divide the modulation scan by the chopped scan to provide R as a function of wavelength.

Typical scans of $R(\lambda)$ are shown in Figure 19 over the range of 1.1 to 4.5 μm. The curves are in serious disagreement with theory in at least two respects. First, according to Equation (1), $R(\lambda)$ should always have the same sign for a given lock-in amplifier phase setting. In Figure 18, $R(\lambda)$ has both positive and negative excursions. Second, the oscillations in $R(\lambda)$, determined by the $\sin^2 (\Gamma/2)$ factor in Equation (1), should coincide with those found in the channel spectrum which, according to theory, also varies as $\sin^2 (\Gamma/2)$. The experimental channel spectrum for the same sample is shown in Figure 20. This was measured with the polarizer orientation, as shown in the figure. Close examination of the curves in Figures 18 and 19 show that the $R(\lambda)$ oscillations are shifted to the right for $\lambda > 1.6$ μm, relative to the channel spectrum oscillations. For $\lambda < 1.6$ μm, the oscillations seem to be roughly in phase.

Further examination of this sample and one other showed that the $R(\lambda)$ curve could be raised or lowered (i.e., the positive to negative crossover points changed) by directing the light through different portions of the sample. Also, the $R(\lambda)$ curves could be similarly distorted (to a smaller extent) by changing the drive voltage.

•The dependence of $R(\lambda)$ on position implies that the sample is not homogeneous. This conclusion was supported by subsequent x-ray topography studies which show distinct variations in crystal structure within the top ~1 μm of the sample. If these variations extend further into the crystal they could explain the anomalous results.

Simple models of polycrystalline structures have been examined to see if the features exhibited by Figure 18 could be reproduced. We have shown that a change in sign of $R(\lambda)$ can come about if two different crystal orientations, e.g., back-to-back twins, exist within a sample. Thus, if two equally thick regions are found in contact with their z-axes parallel, one with a (100) orientation and the other a (110), R will change sign as the wavelength is varied. These calculations show qualitatively that the anomalous behavior could be caused by a non-uniform crystal structure.

12136-2
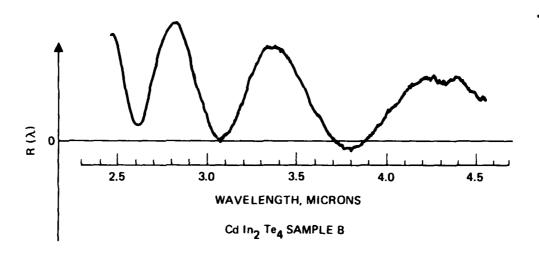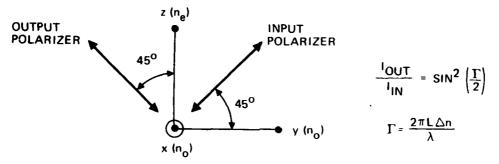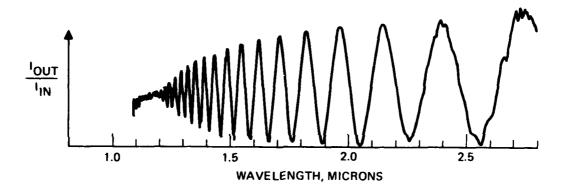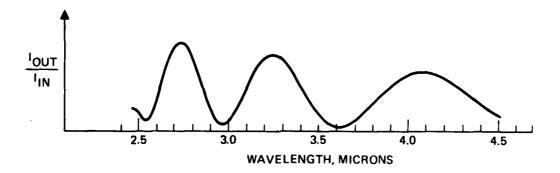
Figure 19. Experimental scans of $R(\lambda)$.

40

$$\frac{I_{OUT}}{I_{IN}} = SIN^2 \left(\frac{\Gamma}{2}\right)$$

$$\Gamma = \frac{2\pi L \Delta n}{\lambda}$$

CdIn$_2$Te$_4$ SAMPLE B

Figure 20.   Experimental channel spectrum.

41

On this basis, calculating r_{41} using Equation (3) results in a value for r_{41} of approximately 50×10^{-12} m/V. This number is more than an order of magnitude larger than that found in $AgGaS_2$. Thus, $CdIn_2Te_4$ promises to be a very attractive candidate at least for electro-optic tunable filters.

d. Analysis of $CdIn_2Te_4$ E-O Measurements

Initial measurements of the electro-optic effect in several test samples of $CdIn_2Te_4$ have produced anomalous results in some wavelength regions where the phase of the detected output signal has changed sign with respect to the driver signal. In an effort to explain this anomaly, we postulated the existence of twinning, wherein one portion of the test platelet has <100> orientation and the other has <110> orientation. Such a hypothetical model is shown in Figure 21. Here we show two zones having the indicated orientations of lengths ℓ_1 and ℓ_2, respectively. The operative EO coefficients are indicated as r_{41} and r_{42}. Other relevant parameters are the resistivity, ρ, optical phase shift, Γ, due to the static birefringence, and the field-dependent rocking angle, α, of the optic axis.

Omitting a rather lengthy and tedious derivation, we can show that the optical transmittance, τ, is given by

$$\tau = 1/2 + (\cos \Gamma_2 - \cos \Gamma) \, \alpha_1 + (1 - \cos \Gamma_2) \, \alpha_2 , \qquad (4)$$

where

$$\Gamma \equiv \Gamma_1 + \Gamma_2 . \qquad (5)$$

Experimentally, the phase-sensitive detected signal is proportional to the derivation of τ with respect to the driving field. Figure 22 shows the expected signal.

$$\frac{d\tau}{dE} \approx 2 \cos \Gamma_2 - \cos \Gamma - 1 , \qquad (6)$$

42
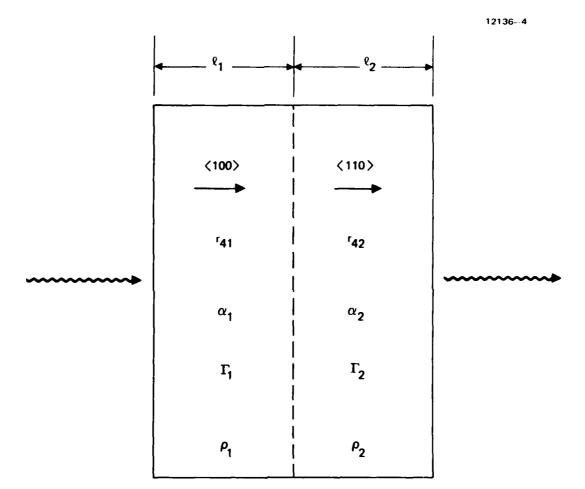
Figure 21. Hypothetical crystal orientation.

43
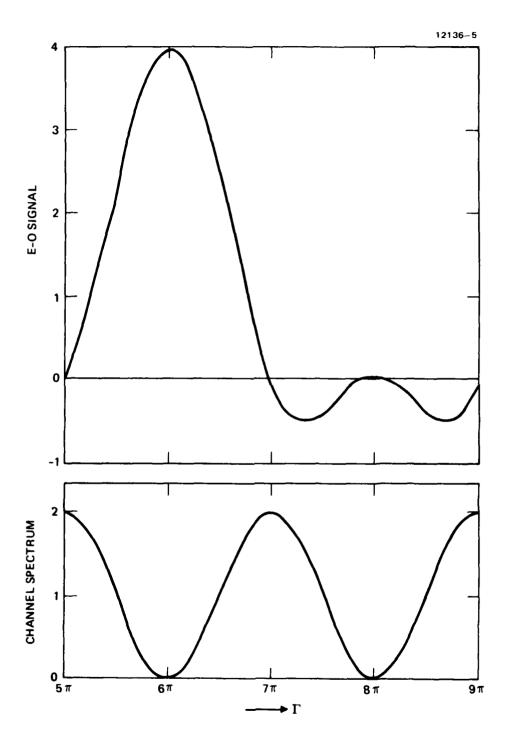
Figure 22. Signal and channel spectrum as a function of optical phase shift.

44

as a function of wavelength, or Γ, in the range 5π to 9π for the assumed conditions,

$$\Gamma_2 = \Gamma_1 \quad , \tag{7}$$

$$\alpha_2 = -\alpha_1 \quad . \tag{8}$$

Also shown is the corresponding channel spectrum,

$$1 - \cos\Gamma \left(\text{equivalent to } 2 \sin^2 \frac{\Gamma}{2}\right) . \tag{9}$$

It is clearly evident that the phase of the signal does indeed change sign, indicating qualitatively that our model is plausible. We note also a shift of phase between the two types of signals.

f. **Measurements of Electro-Optic Coefficients: r_{13} and r_{63}**

We have made preliminary measurements of the electro-optic coefficients r_{13} and r_{63} in $CdIn_2Te_4$ at wavelengths of 3.39 μm and 1.15 μm. Together with these measurements we have also determined the approximate values of the refractive indices at these wavelengths. The results are shown in Table 3. The values of the EO coefficients are as yet approximate due to possible imperfections (e.g., twinning) in the sample tested. These measurements will be repeated at a later time when new, improved crystal samples are prepared.

Table 3. Measured Values of Electro-Optic
Coefficients and Refractive Indices
in $CdIn_2Te_4$ at λ = 3.39 μm and 1.15 μm.
(Applied Field Parallel to Optic Axis)

λ, μm	n	r_{13}, pm/V	r_{63}, pm/V
3.39	2.85	0.15	5.53
1.15	3.12	0.15	5.24

Theory

Diagonalization of the electro-optic impermeability tensor for electric field applied in the z-direction in $CdIn_2Te_4$ (symmetry group 4) leads to the following results:

- Fast and slow axes are induced in the x-y plane, rotated by an angle, α, with respect to the principal axes, where

$$\tan 2\alpha = r_{63}/r_{13} \quad . \tag{10}$$

- The effective electro-optic coefficient is

$$r_{eff} = \sqrt{r_{13}^2 + r_{63}^2} \quad ; \tag{11}$$

that is, the induced phase retardation, Γ_m, between the fast and slow components is
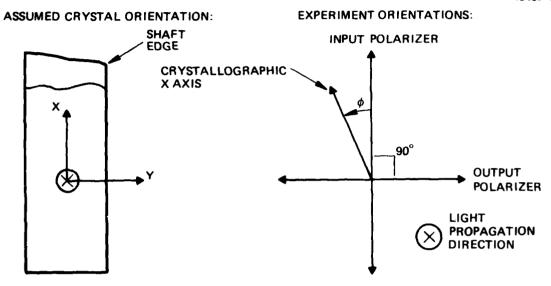
$$\Gamma_m = \frac{2\pi}{\lambda} n^3 \sqrt{r_{13}^2 + r_{63}^2} \, Vm \quad , \tag{12}$$

where V_m is the applied voltage, or field-length product, for longitudinal mode EO operation.

Note that if $r_{13} = 0$, Equation (10) shows that $\alpha = 45°$, which is the well known case with $\overline{4}2m$ crystals, e.g., KDP.

Measurements

With an electric field applied to transparent (ITO) electrodes on the (001) faces, a basal-cut $CdIn_2Te_4$ sample was placed between crossed polarizers, as shown in Figure 23. The sample was mounted on a rotation stage allowing rotation through a complete 2π angle with respect to its initial orientation parallel to the polarizer/analyzer axes. A beam from a He-Ne laser, circularly polarized by means of the Babinet-Soleil compensator, was transmitted through the sample, through the analyzer, some attenuator screens, and finally to a detector element (InSb for 3.39 µm, and a photomultiplier for 1.15 µm).

ASSUMED CRYSTAL ORIENTATION:

SHAFT EDGE

CRYSTALLOGRAPHIC X AXIS

X

Y

EXPERIMENT ORIENTATIONS:

INPUT POLARIZER

ϕ

90°

OUTPUT POLARIZER

LIGHT PROPAGATION DIRECTION

ATTENUATOR SCREENS

SAMPLE ON ROTATION STAGE

CHOPPER

BABINET–SOLEIL COMPENSATOR

InSb DETECTOR

He–Ne LASER

OUTPUT POLARIZER

INPUT POLARIZER
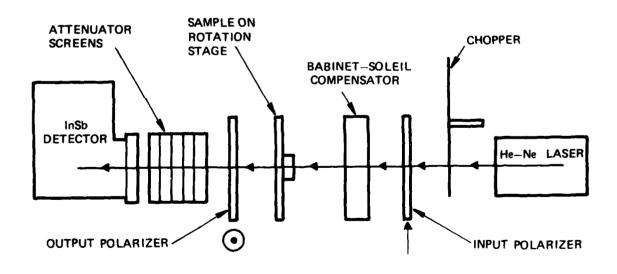
Figure 23. Experimental arrangement for measurement of r_{13} and r_{63} in $CdIn_2Te_4$.

The relative transmission, I_{out}/I_{in}, with this arrangement, as a function of the angle $\Theta = \phi + \alpha$, can be shown to be

$$I_{out}/I_{in} = 1/2 \ (1 + \Gamma_m \sin 2\Theta) \ . \tag{13}$$

Figure 24 shows the variation of the detected signal with Θ, using a square wave voltage, 4 V peak-to-peak, and phase sensitive detection at $\lambda = 3.39$ μm.

It proved to be most sensitive to measure the null points of the signal to establish the orientation angle, α. Four such null points were measured, leading to

$$\alpha = 44.2° \pm 0.5° \ . \tag{14}$$

Thus,

$$r_{63}/r_{13} \ \tan 2\alpha = 35.8 \ . \tag{15}$$

By measuring the relative transmission at the four peak positions, the phase retardation, or modulation index, Γ_m, was determined:

$$\Gamma_m = (4.75 \pm 0.15) \times 10^{-3} \ . \tag{16}$$

Using Equation (12), we obtained at $\lambda = 3.39$ μm,

$$r_{eff} = 5.53 \ pm/V,$$

$$r_{13} = 0.15 \ pm/V,$$

and

$$r_{63} = 5.53 \ pm/V$$
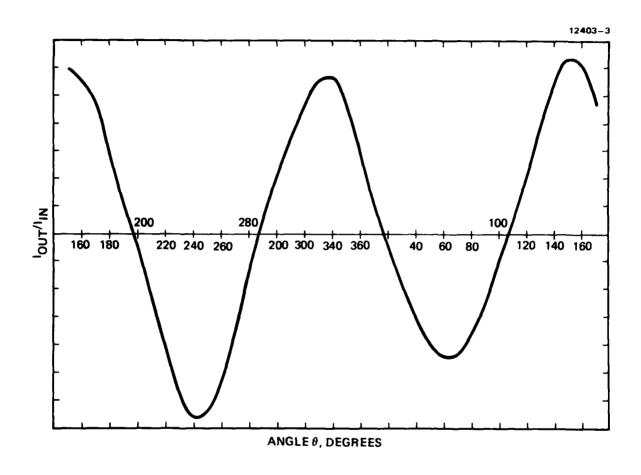
Figure 24.   Variation of detected signal, due to EO modulation as a function of rotation angle, $\Theta \equiv \phi + \alpha$.

Similar measurements using the 1.15-µm He-Ne laser line gave the results shown in Table 3.

The average index of refraction, n, measured at the two wavelengths was determined from direct transmittance of the sample. Allowing for multiple internal reflections, but without coherent superposition, the transmittance is

$$\tau = \frac{2\bar{n}}{\bar{n}^2 + 1} \quad . \tag{17}$$

Thus, solving for $\bar{n}$,

$$\bar{n} = \frac{1}{\tau} + \sqrt{(1/\tau)^2 - 1} \quad . \tag{18}$$

Measured transmittances yielded the index value appearing in Table 3.

B. SYNTHESIS OF NEW TERNARY CHALCOGENIDE COMPOUNDS

As part of this investigation we attempted to synthesize (in addition to $CdIn_2Te_4$) several new ternary chalcogenide compounds, including $AgGaTe_2$, $ZnGa_2S_4$, $CdGa_2S_4$, $ZnIn_2Se_4$, and $ZnIn_2Te_4$. The variations in physical properties of these compounds introduce a variety of obstacles in completing the reactions to form the ternary compound from either the constituent elements or the binary end member constituents, e.g., ZnS, Ga_2S_3, even with excesses of one component for off-stoichrometric solution growth. Some have very high melting points, e.g., $ZnGa_2S_4$, which is reported to melt above 1300°C. Others have highly volatile elemental and binary constituents, e.g., Zn, Cd, ZnS, and CdS. These properties require the use of several different reaction/synthesis techniques:

- Solid-liquid phase reaction — In this method, the components are introduced into a short ampoule, which is evacuated and sealed. The ampoule is lowered through a thermal zone which is usually higher in temperature than the melting point of the desired compound. Low melting constituent elements or compounds initiate the reaction and enhance the reaction rate.

50

- **Vapor-liquid phase reaction** — This synthesis is typically carried out by reacting the molten metals contained in a boat in a closed evacuated ampoule. The chalcogenide vapor is introduced into the reaction zone from the cold end of the ampoule by slowly increasing its temperature. A rocking furnace enhances mixing of the components and allows the reaction to go to completion.

- **Vapor phase reaction** — When constituent elements or intermediate compounds containing some of the constituents have high vapor pressures, the reaction to form a ternary compound can occur by reaction of the vapor species. This is a difficult process to safely complete, especially when there are significant differences in vapor pressures of the species. The ampoule must be heated slowly to permit reaction to take place before significant pressure build-up occurs. In addition, the heating must be uniform to prevent condensation of intermediate (transient) phases.

All of these reaction techniques have been used in this laboratory as part of this program to synthesize new materials and are discussed below.

1. $AgGaTe_2$

The first method discussed above, solid-liquid phase reaction, has been used successfully for the synthesis of $AgGaTe_2$ which has a low melting point that permits reaction to occur without any significant pressure buildup. The low melting point of gallium enhances the reaction. In this case, reaction and subsequent in situ crystal growth can be accomplished by using an off-stoichiometric composition similar to the way we have grown single crystals of $CdIn_2Te_4$ previously described in this report.

Polycrystalline ingots of $AgGaTe_2$ were grown from the melt using the Bridgman-Stockbarger technique. $AgGaTe_2$ is an incongruently melting chalcopyrite, and the existence region has not been studied in detail. Successful synthesis of $AgGaTe_2$ has been achieved from a Ga_2Te_3-rich solution. However, our measurements, as discussed below, indicate the possibility of variations in stoichiometry or an additional phase within the ingot.

Recent studies at HRL using differential thermal analysis (DTA) indicate that the phase diagram (Figure 25) reported in the literature[14] is generally correct on the $AgTe_2$-rich regions around the compound $AgGaTe_2$ (β in the diagram). However, our findings (Figure 26) indicate that crystallization from the Ga_2Te_3-rich side is possible within a short temperature range, but crystals invariably contain an additional phase which we could not identify. In addition, the slopes of the liquidus and solidus curves on the Ga_2S_3-rich side are very flat, leaving only a small T-X region to work in which to obtain single crystal growth. Our investigation by DTA of the Ag_2Te-rich side of the phase diagram indicates that it is more promising for single crystal growth of $AgGaTe_2$.

A 0.5-in.-diameter boule, grown by the Bridgman-Stockbarger technique, was found to be polycrystalline along its entire length. The x-ray diffraction pattern for $AsGaTe_2$ is shown in Figure 27. A few large pieces were mined out for dielectric measurements. The average dielectric constant, measured at 1 MHz for this material, was 270 (Table 2). However, there were large variations in the measurement from sample to sample (nearly 35%), indicating either variations in stoichiometry or the presence of an additional phase. An IR transmission measurement (Figure 28) showed transmission of ~40% (uncorrected for Fresnel losses) at 2.5 μm, decreasing in a manner typical of free-carrier absorption, becoming opaque beyond 4.5 μm. From its composition and relationship to other chalcopyrites, transmission further out in the IR would be expected. DC resistivity for $AgGaTe_2$ was measured to be as high as 6×10^7 Ω-cm on some samples.

In a subsequent run, an ingot of $AgGaTe_2$ was grown from a melt composition which consisted of 40% Ga_2Te_3 and 60% Ag_2Te; the starting point, both in composition and temperature (800°C), is shown by X in the pseudo binary phase diagram in Figure 25. Crystal growth is initiated at the line a-a' where the solid $AgGaTe_2$ is in equilibrium with the liquid (composition at a).
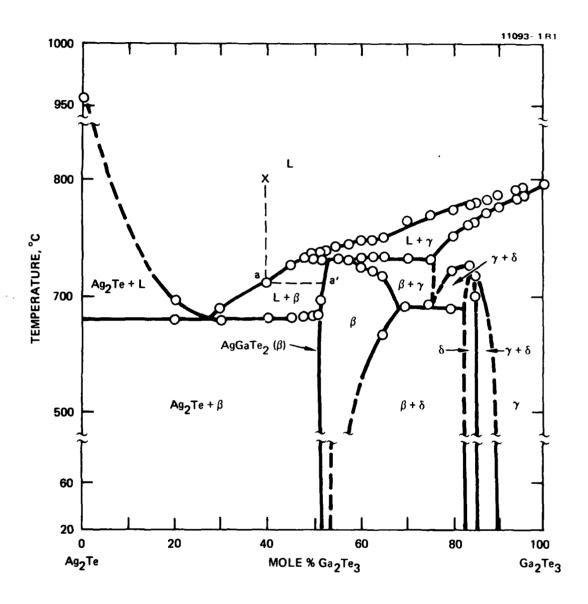
Figure 25. The system $Ag_2Te-Ga_2Te_3$. (From Palatnik and Belova, 1967. Reference 5.)
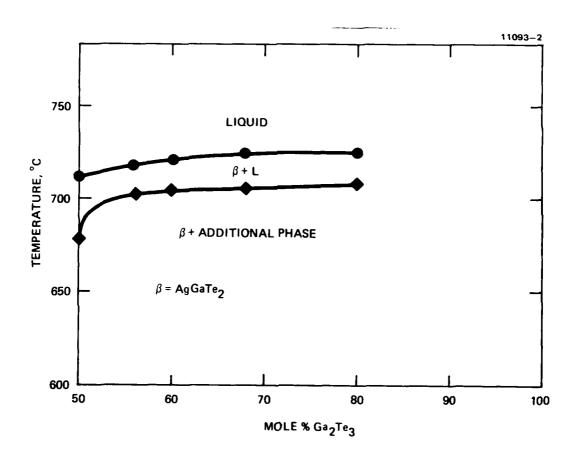
Figure 26. Phase diagram of section of system $Ag_2Te-Ga_2Te_3$ derived from DTA.
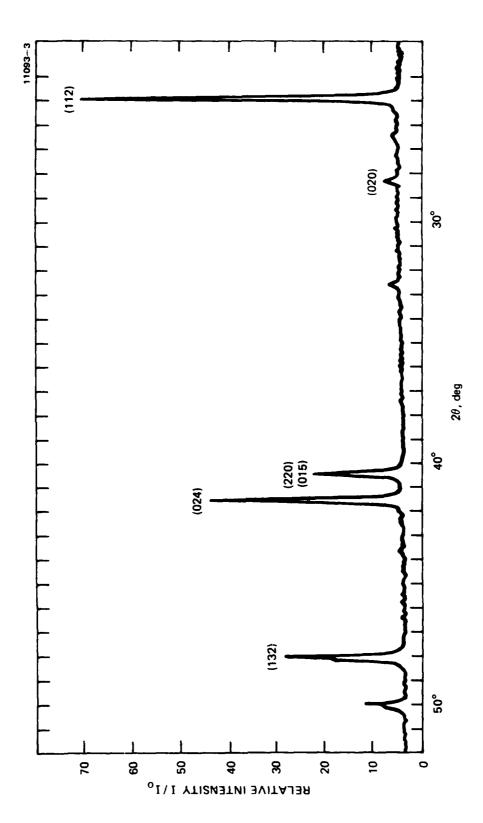
Figure 27. X-ray diffraction pattern for AgGaTe$_2$.
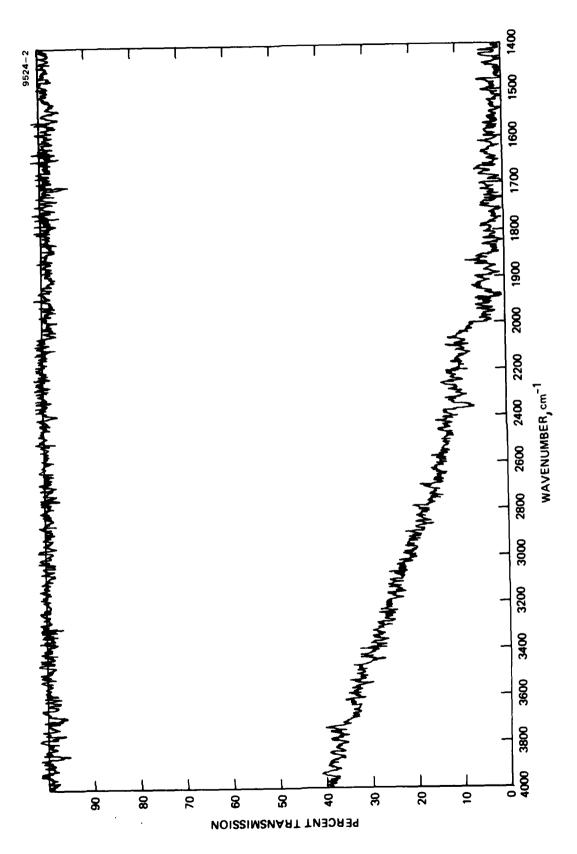
Figure 28. IR transmission spectrum for $AgGaTe_2$.

56

Borshchevsky[13] has shown that the composition line for $AgGaTe_2$ is essentially straight in this region — not as indicated in the published diagram. The growth rate used was 0.5 mm/hr. The ingot was polycrystalline with submillimeter grains.

No single crystals of significant usable size of $AgGaTe_2$ were grown during the course of this program.

2. Additional Ternary Chalcogenides of the Type $A^{II}B_2^{III}C_4^{VI}$

The vapor-liquid phase reaction has been used to synthesize $ZnIn_2Se_4$ and $ZnIn_2Te_4$. In these cases, Zn and In are mixed in stoichiometric proportion in a boat, melted, and subsequently reacted with the chalcogenide, which is, in turn, introduced as a vapor by slowly pushing the cool end of the tube into the hot zone of the furnace. The procedure lasted approximately 15 hours and yielded a large amount of the ternary compound. The reaction, however, was not complete and some intermediate reaction products, e.g., ZnSe, In_2Se_3, ZnTe, and In_2Te_3 remained. The x-ray data (Figure 29) indicate great similarities between the ternary compound and the II-VI binary. This has caused some concern of the completeness of the reaction. An investigation using Guinier techniques revealed the presence of some ZnSe and In_2Se_3. We are pursuing this to determine quantitatively the degree of completion of the reaction. The products will be remixed and reacted once more to ensure that no additional phases are present.

We have investigated the vapor phase reaction technique for compounds such as $CdGa_2S_4$ and $ZnGa_2S_4$, which have relatively high melting points and where intermediate compounds, e.g., ZnS, CdS, Ga_2S_3, have significant vapor pressures at elevated temperatures. We have approached the synthesis/reaction using both elements and intermediate compounds as starting materials. The approach using elemental constituents for $CdGa_2S_4$ has been successful. However, we have experienced condensation of these phases in cool portions of the ampoule as well as an explosive build-up of pressure. Runs lasting as long as 11 days at 1050°C have, at times, shown little or no reaction, the resulting products being ZnS or CdS and Ga_2S_3.

Attempts were made to synthesize samples of $ZnIn_2S_4$. $ZnIn_2S_4$ is particularly interesting because it belongs to the same point group (3M) as $LiNbO_3$ and contains a fraction of the indium atoms in octahedral coordination.

57

	ZnTe		$ZnIn_2Te_4$	
hkl	d(Å)	I/Io	d(Å)	I/Io
100/112	3.523	100	3.53	70
200	3.051	10	3.05	20
220	2.159	80	2.163	100
311/312	1.840	35	1.847	80
400	1.526	8	1.530	40
331/332	1.400	14	1.405	70
422/424	1.2456	10	1.250	80
LATTICE CONSTANTS				
a	6.1026		6.122	
c	6.1026		12.244	
c/a	1.0000		2.000	

Figure 29. X-ray diffraction data for ZnTe and $ZnIn_2Te_4$.

Our approach involved the reaction of the molten metals with sulfur in a rocking furnace. Initial attempts were not successful.

Two compounds containing Zn, In, and S were identified as reaction products by x-ray powder diffraction techniques: $Zn_3In_4S_9$ and $Zn_9In_8S_{21}$. The powder diffraction pattern for these compounds is shown in Figure 30.

C. OTHER TERNARY COMPOUNDS ($ZnGeP_2$ and $AgGaS_2$)

Our previous knowledge and experience in the synthesis and crystal growth of ternary compounds having the chalcopyrite structure led us to grow crystals of $ZnGeP_2$ and $AgGaS_2$. The family of compounds of the type $A^{II}B^{IV}C^V_2$ has been of interest because of the potential for large non-linear coefficients; the largest has been measured in samples of $CdGeAs_2$ but this crystal has not been successfully grown in larger than millimeter sizes. The ternary chalcogenide chalcopyrite, $AgGaS_2$, is interesting for the investigation of its properties relating to acousto-optic and SAW devices since it is the ternary derivative of Group II sulfides, e.g., CdS, wherein a Group I and a Group III element alternately substitute for the Group II element. This substitution doubles the unit cell dimension in the c-axis direction, thus yielding a tetragonal crystal lattice.

$ZnGeP_2$ was synthesized by reaction of the elements as described in reference 15. Using the pre-reacted material, crystal growth proceeded by a vertical Bridgman-Stockbarger technique. The compound melts at approximately 1020°C; no phase transitions were observed in the solid upon cooldown or by DTA. An infrared transmission spectrum of a crystal indicated a short wave cutoff of approximately 1.4 micrometers and a long wave cutoff of 13 micrometers.[15] Although the crystal showed theoretical transmission (uncoated, uncorrected for Fresnel losses) of nearly 58% in the range of 3 to 8 µm, some structure was observed in the far IR portion of the spectrum indicating the possibility of impurity absorption in these regions. The non-linear coefficient has been reported[16] to be $d_{14} = 2.7 \times 10^{-7}$ cgs or 111×10^{-12} m/V. These measurements are reported within an accuracy of 30% and were not reconfirmed during the course of this program. Phase-matched sum mixing of 10.6 µm and 1.6 µm has been reported previously.[17]

Figure 30. X-ray diffraction pattern of $Zn_3In_4S_9$ [x] and $Zn_9In_8S_{21}$ [o].

60

$AgGaS_2$ was synthesized by reaction of the constituent elements in a rocking furnace; the sulfur is introduced as a vapor above the molten metals in stoichiometric proportion at 1050°C. Rocking perturbs the molten floating layer of $AgGaS_2$ on top of the metals and thereby allows further reaction with the sulfur to continue. The compound is subsequently zone-refined for purification and stabilization of the maximum melting composition. Crystal growth is carried out using material which has undergone four zone passes mixed with additional Ag_2S to grow slightly on the Ag_2S-rich side of the existence region. The maximum melting point occurs at approximately 1006°C; the addition of Ag_2S lowers the melting point slightly. Single crystals are grown using the seeded Bridgman technique. As-grown samples have resistivities of the order of 10^{12} ohm-cm. Transmission spectra show theoretical transmission from approximately 0.6 to 12 μm. We determined the electro-optic coefficient, $r_{41} = r_{52}$, to be approximately 3.6 pm/V. Properties of this material pertinent to SAW devices have not been investigated. Our plan to determine the stress-optic coefficients using anisotropic transmission ellipsometry was not completed during the course of this program.

SECTION 4

THEORETICAL MODEL: ELECTRO-OPTIC EFFECT IN CRYSTALS

During the DARPA program, a parallel effort was pursued by Professor Amnon Yariv and Dr. C. Shih, Applied Physics Department at Caltech, to develop a theoretical model for the EO effect in coordination with the structural analog concepts pursued in this program. The prime motivation of the theoretical effort was to obtain an expression that could be used to calculate and predict the EO coefficient of new crystals. By applying the localized bond charge model of Phillips and Van Vechten,[18-19] which attributes the dielectric response of covalent crystals to the localized bond charge, Yariv and Shih[7] have developed a method for calculating the EO tensor coefficients. Comparisons with experimental values for binary compounds having zincblende and wurtzite structures were excellent. Recently, the calculations have been extended to ternary compounds (Table 4) with equally good results.

Table 4. Results for $LiNbO_3$ and $LiTaO_3$

	$LiNbO_3$		$LiTaO_3$	
ε_{dc3}	28		43	
$\varepsilon_{dc1,2}$	43		41	
$\varepsilon_c^*/\varepsilon$	1.8		2.0	
	Nb-O (Short)	Nb-O (Long)	Ta-O (Short)	Ta-O (Long)
$2r_o$	1.889 Å	2.112	1.891	2.071
f_i	0.821	0.830	0.847	0.853
$-f$	0.292	0.241	0.282	0.238
	r_{33}	r_{51}	r_{33}	r_{51}
r_{ionic}	+19.9	+19.7	+27.8	+16.5
r_{elec}	+ 6.0	+ 0.8	+ 3.70	+ 0.24
theo r_{sum}	+25.9	+20.5	+31.5	+16.7
r_{exptl}	+28	+23	+30	+15

7209

63

SECTION 5

PHOTO-ELASTIC MODEL

To model the acousto-optic effect or photoelastic effect, we shall start with an index ellipsoid method of calculating the effective index of refraction as a function of direction of propagation. The index ellipsoid can be written as

$$1 = E\left(\frac{1}{n_{ij}}\right)^2 . \tag{19}$$

In the principal coordinates system, the cross terms vanish, leaving,

$$1 = \left(\frac{1}{n_{xx}}\right)^2 + \left(\frac{1}{n_{yy}}\right)^2 + \left(\frac{1}{n_{zz}}\right)^2 . \tag{20}$$

To model the photoelastic effect, one considers first order (linear) changes in the $(1/n_{ij})^2$ components in terms of strains or stresses in the solid. Therefore, we write

$$\Delta\left(\frac{1}{n^2}\right) = P_{ijk\ell} \, S_{k\ell} , \tag{21}$$

where $S_{k\ell}$ is the strain component, and $P_{ijk\ell}$ is its photoelastic constant. In analogy, in the Pockels effect (linear electro-optic effect), we write,

$$\Delta\left(\frac{1}{n_{ij}}\right)^2 = r_{ijk} \, E_k^{(o)} , \tag{22}$$

where the polarization in its ith direction is,

$$P_i = C_i \, r_{ijk} \, E_j^{(\omega)} E_k^{(o)} . \tag{23}$$

In the elasto-optic case, we may write the ith component of the polarization as

$$P_i = C_2 P_{ijk\ell} E_j^{(\omega)} S_{k\ell}^{(o)} \quad . \tag{24}$$

In order to examine the source of this polarization, we consider the individual bonds. For bonds i and $\mu(i) = \chi^{(i)} E^{(\omega)}$,

i = bond direction χ, $^{(i)}$ the bond susceptibility, and

α_β^i $_{(\beta=1,2,3)}$ are the direction cosines of the ith direction bond.

Thus,

$$E_i = \vec{E} A_i = \left(E_x \hat{x} + E_y \hat{y} + E_z \hat{z} \right) \cdot \left(\alpha_1^{\ i} \hat{x} + \alpha_2^{\ i} \hat{y} + \alpha_3^{\ i} \hat{z} \right)$$

$$= \sum_s \alpha_s^{(i)} E_s^{(\omega)} \quad , \tag{25}$$

and

$$\mu(i) = \chi^{(i)} \alpha_s^{(i)} E_s^{(\omega)} \quad . \tag{26}$$

Now we can express P_i in terms of a sum over the individual bonds, where N = number of unit cells per volume = $1/\Omega$ and Ω = volume of the unit cell:

$$P_i = N \sum_i \sum_s \alpha_s^{(i)} \alpha_j^{(i)} \chi^{(i)} E_s^{(\omega)} \quad , \tag{27}$$

$$\frac{\Delta P_i}{S_{k\ell}} = \sum \sum \alpha_s^{(i)} \alpha_j^{(i)} \alpha\chi^{(i)} E_s^{(\omega)} \quad , \tag{28}$$

and

$$\frac{\partial P_i}{\partial S_{k\ell}} = N \left\{ \sum_i \sum_s \alpha_s^{(i)} \alpha_j^{(i)} \frac{\partial \chi^{(i)}}{\partial S_{k\ell}} \varepsilon_s^{(\omega)} \right. \tag{29}$$

$$+ \sum_i \sum_s \left(\alpha_s^{(i)} \frac{\partial \alpha_j}{\partial S_{k\ell}} + \frac{\partial \alpha_s}{\partial S_{k\ell}} \alpha_j^{(i)} \right) \chi^{(i)} \varepsilon_s^{(\omega)} ,$$

$$+ \frac{\partial N}{\partial S_{k\ell}} \sum_i \sum_s \alpha_s^{(i)} \alpha_j^i \chi^{(i)} \varepsilon_s^{(\omega)} \left. \right\} ,$$

where

$$N = \frac{1}{V} \quad \frac{\partial N}{\partial S_{k\ell}} = -V^{-2} \quad \frac{\partial V}{\partial S_{k\ell}} \quad . \tag{30}$$

Now

$$\frac{\Delta V}{V} = S_{k\ell} \, \alpha_{k\ell} \tag{31}$$

because shear waves do not change the volume; therefore,

$$\frac{\partial N}{\partial S_{k\ell}} = - \frac{1}{V^2} \frac{\partial V}{\partial S_{k\ell}} = - \frac{1}{V^2} V \, \alpha_{k\ell} \tag{32}$$

$$\frac{\partial N}{\partial S_{k\ell}} = - \frac{\alpha_{k\ell}}{V} \quad . \tag{33}$$

From Equations (20) and (21) we obtain

$$\Delta P_j = N \left\{ \sum_{\substack{i(\text{unit} \\ \text{cell})}} \sum_{s=1,2,3} E_s^{(\omega)} \left| \alpha_s^{(i)} \alpha_j^{(i)} \frac{\partial \chi^{(i)}}{\partial S_{k\ell}} \right. \right.$$

$$\left. + \chi_i \left(\alpha_s^{(i)} \frac{\partial \alpha_j}{\partial S_{k\ell}} + \alpha_j^{(i)} \frac{\partial \alpha_s}{\partial S_{k\ell}} \right) \right|$$

$$\left. - \frac{\alpha_{k\ell}}{V} \sum_i \sum_s \alpha_s^{(i)} \alpha_j^{(i)} \chi^{(i)} E_s^{(\omega)} \right\} ; \qquad (34)$$

but

$$\Delta P_j = - \frac{\epsilon_{jj} \epsilon_{ss}}{\epsilon_o} P_{ijk\ell} S_{k\ell} E_s^{(\omega)} . \qquad (35)$$

Therefore, we can identify the elasto-optic coefficient as:

$$P_j S_{k\ell} = \left| - \frac{N\epsilon_o}{\epsilon_{jj} \epsilon_{ss}} \sum \underbrace{\alpha_s^{(i)} \alpha_j^{(i)} \frac{\partial \chi^{(i)}}{\partial S_{k\ell}}}_{A} + \underbrace{\chi^i \alpha_s^{(i)} \frac{\partial \alpha_j}{\partial S_{k\ell}} + \alpha_j^{(i)} \frac{\partial \alpha^{(i)}}{\partial S_{k\ell}}}_{B} \right.$$

$$\left. + \frac{\alpha_{k\ell}}{V \epsilon_{jj} \epsilon_{ss}} \underbrace{\sum_i \alpha_s^{(i)} \alpha_j^{(i)} \chi^{(i)}}_{C} \right| . \qquad (36)$$

Terms A and C in the above expression correspond to an elasto-optic effect that is linear in the strain. This is the normal elasto-optic effect. However, the B term in the above expression, which gives rise to a quadratic elasto-optic effect, corresponds to rotation of bonds which could be a large effect. However, this has not yet been observed.

68

SECTION 6

OPTICAL EVALUATION OF CRYSTALS

A. MEASURING STRESS OR STRAIN INDUCED ANISOTROPY IN SINGLE-CRYSTAL MATERIALS

The technique usually used for measuring the optical anisotropy or bierefringence induced in a single crystal by applying stress to the crystal is dual-beam interferometry. In this technique the optical beam is split into two beams. which are passed through two samples of the same material. When stress is applied to one sample the optical index changes, causing the phase of the beam in that arm to change and the interfering beams produce a shift in the fringe pattern. If a careful measurement is made of the fringe shift, then this quantity can be used to evaluate the stress-optic of the elasto-optic constants of the material. For example, the stress-optic the elasto-optic effects are given approximately by the following expressions:

$$\Delta N = 1/2(N_o)^3 \, q_{ij}\sigma_j \quad , \tag{37}$$

and

$$\Delta N = 1/2(N_o)^3 \, P_{ij}\varepsilon_j \quad , \tag{38}$$

where N_o is the ordinary refractive index of the medium, q_{ij} and P_{ij} are the stress optic and elasto-optic constants of the medium, and σ and ε are the applied stress and the resultant strain. These equations can be evaluated to estimate the change in index due to an applied force. For example, if the refractive index of the medium is 2.5 and the stress optic constant is 10^{-11} cm^2/dyne, then a force of 1 lb (4.5×10^5 dynes) applied across a 1 mm square cross section sample will produce a change in index of

$$\Delta N = 1/2 \, (2.5)^3 (2 \times 10^{-11}) \times 4.5 \times 10^7 = 7 \times 10^{-3} \quad . \tag{39}$$

This corresponds to a change in phase of

$$\Delta\phi = \frac{2\pi}{\lambda}T \, \Delta N = \frac{6.28}{0.632 \times 10^{-6}} \times 10^{-3} \times 7 \times 10^{-3} = 69.6 \text{ radians} = 3985° \quad , \tag{40}$$

or to a shift of 11 fringes. If the same force were applied across a 10 mm square cross section, we would get a phase shift of 0.7 radians and a corresponding shift of 0.11 fringes. If the sample is thicker than 1 mm then these fringe shifts are correspondingly larger. If the samples are not mechanically strong, the the applied force must be restricted to lower values and the thickness of the samples must be increased.

If the crystals have a relatively high refractive index, then the possibility of multiple propagation or multiple reflection effects can occur. These effects can significantly alter the phase of the transmitted waves and they can lead to errors in the determination of the stress optic and elasto-optic constants. For this reason we have analyzed the phase changes introduced into a polarized beam propagating in an anisotropic medium in a later section.

The method for the measurement of the photoelastic constants of materials used by the National Bureau of Standards is given below. In this system (see Figure 31) an unpolarized light beam passes through a Wollaston prism which separates the two polarization components. The vertically polarized component is not deflected by the prism and it passes down the axis of the system through a $\lambda/4$ wave plate to a mirror which retro-reflects the beam. This beam passes through the $\lambda/4$ wave plate a second time and exits as a horizontally polarized wave, which passes back through the Wollaston prism and is then deflected as an output beam. The horizontally polarized component of the input beam is deflected by the Wollaston prism and it is recollimated by a lens and passed through the sample, the $\lambda/4$ wave plate, reflected from the mirror and back through the optical system including the wave plate, the two lenses, and the Wollaston prism. The double passage through the wave plate rotates the polarization so that the sample beam exits the Wollaston prism undeflected and collinear with the reference beam. These two beams now interfere to produce a set of interference fringes which shift as stress is applied to the sample. If the orientation of the Wollaston prism is rotated by 90°, the elasto-optic effect for the orthogonal polarization is observed. Using this set of fringe shifts and the applied stress values, the elasto-optic constants of the materials can be measured using the theoretical expressions derived below.

70

STRESS

λ/4
PLATE

SAMPLE

LENS

WOLLASTON
PRISM

OUTPUT
BEAM

H

V

INPUT
BEAM

MIRROR

POLARIZER
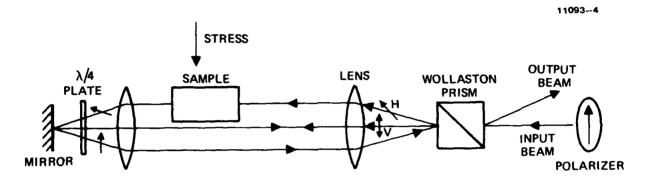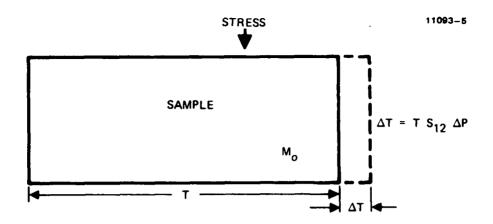
Figure 31.   Interferometer for measuring stress induced change in optical
path length.

71

STRESS

SAMPLE

M_0

$\Delta T = T\ S_{12}\ \Delta P$

T

ΔT

The optical phase difference before applying stress is given by

$$\Delta\phi_1 = \frac{2\pi}{\lambda}\ TN_0 - \frac{2\pi}{\lambda}\ T = \frac{2\pi}{\lambda}\ T(N_0 - 1)\ .\tag{41}$$

The optical phase difference after applying stress is given by

$$\Delta\phi_2 = \frac{2\pi}{\lambda}(T + \Delta T)(N_0 + \Delta N_0) - \frac{2\pi}{\lambda}\ (T + \Delta T)\ .\tag{42}$$

The net phase change $\Delta\phi = \Delta\phi_2 - \Delta\phi_1$ corresponds to a fringe shift, $\Delta N = \Delta\phi/2\pi$:

$$\Delta N = \frac{1}{\lambda}\left[(T+\Delta T)(N_0+\Delta N_0) - (T+\Delta T) - T(N_0-1)\right] \cong \frac{1}{\lambda}\left[T\Delta N_0+\Delta TN_0-\Delta T\right].\tag{43}$$

Using the relationships, $\Delta N_1 = N_0^3/2\ q_{11}\ \Delta P$ and $N_1\ N_0^3/2\ q_{12}\ \Delta P$, and solving for q_{11} and q_{12}, we find

$$q_{11} = \frac{2}{N_0^3}\ \lambda\ \frac{\Delta N_1}{\Delta P} + \left(N_0 - 1\right)S_{12}\tag{44}$$

and

$$q_{12} = \frac{2}{N_0^3}\ \frac{\lambda}{T}\ \frac{\Delta N_2}{\Delta P} + \left(N_0 - 1\right)S_{12}\ ,\tag{45}$$

where ΔN_1 is the fringe shift, ΔP is the applied pressure, and S_{12} is an elastic constant. Evaluation of the stress optic constant in this experiment also requires an evaluation of the elastic constants of the material. If we

72

recast these equations in terms of the strain optic coefficients,we can simplify the procedure to

$$\Delta N = \frac{1}{\lambda} \left| T\Delta N_o + \Delta T N_o - \Delta T \right| = \frac{T}{\lambda}\left[\Delta N_o + \left(\frac{\Delta T}{T}\right)\left(N_o - 1\right)\right] . \tag{46}$$

Using the strain optic relation,

$$\Delta N_{10} = \frac{N_o^3}{2} P_{11}\epsilon_1 \text{ and } \Delta N_{20} = \frac{N_o^3}{2} P_{12}\epsilon_2 ; \qquad \epsilon_1 = \frac{\Delta T_1}{T_1} \tag{47}$$

this becomes

$$\Delta N_1 = \frac{T}{\lambda}\left[\frac{N_o^3}{2} P_{11}\epsilon_1 + (N_o - 1)\epsilon_3\right] \tag{48}$$

and

$$\Delta N_2 = \frac{T}{\lambda}\left[\frac{N_o^3}{2} P_{12}\epsilon_1 + (N_o - 1)\epsilon_3\right] . \tag{49}$$

Solving for P_{11} and P_{12}, we obtain the evaluation expression for the elasto-optic constants,

$$P_{11} = \frac{2}{N_o^3}\left[\frac{\lambda}{T} \frac{\Delta N_1}{\epsilon_1} (N_o - 1) \frac{\epsilon_3}{\epsilon_1}\right] \tag{50}$$

and

$$P_{12} = \frac{2}{N_o^3}\left[\frac{\lambda}{T} \frac{\Delta N_2}{\epsilon_2} - (N_o - 1) \frac{\epsilon_3}{\epsilon_1}\right] . \tag{51}$$

The quantity $\epsilon_3 = \Delta T_3/T_3$ is the strain induced in the medium in the direction of propagation of the light, and $\epsilon_1 = \Delta T_1/T_1$ is the strain induced in the medium in the direction of the applied stress. In this case, strain gauges must be applied to the sample to measure both strain parameters. This is experimentally cumbersome.

In comparing relative photoelastic measurements, if two polarized ortho-
gonal beams are sent through the sample and stress is applied parallel to one
polarization, then the relative phase change between the two waves have the
form

$$\Delta\phi = 2\pi(\Delta N_1 - \Delta N_2) = \frac{2\pi T}{\lambda} \left[\frac{N_o^3}{2} (P_{11} - P_{12}) \epsilon_1 + (N_o - 1)\epsilon_3 - (N_o - 1)\epsilon_3 \right] . \tag{52}$$

The fringe shift is given by

$$\Delta N = \frac{\Delta\phi}{2\pi} = \frac{T}{\lambda} \frac{N_o^3}{2} (P_{11} - P_{12}) \epsilon_1 , \tag{53}$$

and the differences between the elasto-optic constants is equal to

$$P_{11} - P_{12} = \left(\frac{\lambda}{T}\right)\left(\frac{2}{N_o^3}\right) \left(\frac{\Delta N}{\epsilon_1}\right) , \tag{54}$$

where ΔN is the fringe shift for materials under uniaxial compression. For
materials such as fused quartz $P_{11}-P_{12} = (0.197-0.088) \approx 0.1$ and $N = 1.46$
at $\lambda = 6328$ Å. For a 1-cm optical path and a strain of 10^{-5},

$$\Delta N = \frac{10^{-2} \text{ m}}{0.6328 \times 10^{-6} \text{ m}} \times \frac{(1.46)^3}{2} \times (0.1) \times 10^{-5}$$

$$= 0.025 \text{ fringes} = 8 \text{ deg} \tag{55}$$

The measurement of 2/100 of a fringe is very difficult unless you use a
technique such as ellipsometry or a Babinet Soliel compensator to convert an
optical-phase change into an optical path change. When measuring infrared
transmissive materials, the refractive indices are usually at least a factor
of two larger than that of quartz, and the fringe shifts will be of the order
of five times larger at the same wavelength. At longer wavelengths the shifts
will be smaller.

These techniques can be directly applied to polycrystalline materials if
they do not disturb the polarization state of the light propagating through

74

the crystal. This can be checked using a crossed polarizer and analyzer to observe the field. If the sample appears variegated or matted, then the beam has been depolarized and a simple interpretation of the effect is not feasible. If the polarization state is disturbed, then part of the elasto-optic effect will be to scatter light back into the original polarization that was scattered out by the randomly oriented crystallites; the other part of the effect will be to modulate the phase of these polarizations. The resultant effects will probably not be simple to interpret, but it is worthwhile to experimentally evaluate the effects of stress applied to a polycrystalline anisotropic rectangle through which polarized light is passing. If large elasto-optic effects are observed then obviously phase cancellation is not important and this approach will be useful for evaluating materials. If it does not work, then we will have to grow single crystals of these materials or we will have to develop techniques for measuring small regions of thinly sliced samples.

B. ANISOTROPIC TRANSMISSION ELLIPSOMETRY

The measurement of anisotropy in crystals can be done by reflection or transmission. If the anisotropy is large then conventional ellipsometry can be used to measure the relative amplitude reflection ratio of the parallel and perpendicular polarization components. If the anisotropy is small, a transmission technique is more pertinent because the long optical path will produce large changes in the relative phase shift of the parallel and perpendicular components. For reasons of analytic simplicity, the transmission experiments are usually conducted at normal incidence. In this case, the waves can undergo multiple reflection between the faces of the sample and the sample acts as a Fabry-Perot filter. The Fabry-Perot effect enhances the relative phase shift due to anisotropy so that the measured phase shift of the two polarization components is larger or smaller than that expected from a single pass. Starting from Born and Wolf[15], p. 323, the expressions for the complex transmission coefficient of a dielectric plate have been recast into the ellipsometer equations for transmission through an anisotropic dielectric

75

plate (see Appendix). These equations show that the measured optical phase shift cannot be used directly for evaluating the anisotropy. Instead, iterative computer calculations will have to be performed to fit the experimental data. The process is similar to ordinary ellipsometry, with the exception that the complex transmission coefficients are different than the reflection coefficients.

In practice, a sample is placed in the beam of a transmission ellipsometer and adjusted until the optic axis lies either in the horizontal or the vertical plane. The instrument is then adjusted for a null in transmission and the parameters Λ and ψ are determined from the instrument readings. These parameters are fed into the computer and an iterative search is performed over a selected range of $N_\parallel$, $N_\perp$ and T to obtain best fits to Λ and then the chosen values $N_\parallel'$ $N_\perp'$ T' and Δ are used to evaluate ψ. There may be numerous values of these parameters which provide the same values of Λ and ψ.

Computer simulation calculations with these equations are required to study the "dispersion" of the equations for different refractive index and index anisotropy ranges as well as for various thickness ranges. These calculations will also be done for various wavelengths to determine if optimum thickness or wavelength regimes exist for performing these measurements. Ideally, one of these sets of calculations will show the same thickness values and index values for each wavelength. In this way the multiple wavelength data can be used to screen out incorrect results. It is even possible to write a program which will evaluate the results of multiple wavelength measurements simultaneously.

C.   DOUBLE REFRACTION AND THE STRESS OPTIC EFFECT

The indicatrix of an anisotropic crystal is given by

$$\frac{X_1^2}{N_1^2} + \frac{X_2^2}{N_2^2} + \frac{X_3^2}{N_3^2} = 1 \quad \text{or} \quad B_1 X_1^2 + B_2 X_2^2 + B_3 X_3^2 = 1 \tag{56}$$

where

$$B_1 = \frac{1}{K_1} = \frac{1}{N_1^{\,2}} \; ; \; B_2 = \frac{1}{N_2^{\,2}} \; ; \; B_3 = \frac{1}{N_3^{\,2}} \; . \tag{57}$$

The matrix equation for terms $\Delta B_i = \pi_{ij}\sigma_j$ when written out for class $\bar{4}$ is

$$
\begin{bmatrix} \Delta B_1 \\ \Delta B_2 \\ \Delta B_3 \\ \Delta B_4 \\ \Delta B_5 \\ \Delta B_6 \end{bmatrix}
=
\begin{bmatrix} B_1' - B_1 \\ B_2' - B_2 \\ B_3' - B_3 \\ B_4 \\ B_5 \\ B_6 \end{bmatrix}
=
\begin{bmatrix}
\pi_{11} & \pi_{12} & \pi_{13} & 0 & 0 & \pi_{16} \\
\pi_{12} & \pi_{11} & \pi_{13} & 0 & 0 & \pi_{16} \\
\pi_{31} & \pi_{32} & \pi_{33} & 0 & 0 & 0 \\
0 & 0 & 0 & \pi_{44} & \pi_{54} & 0 \\
0 & 0 & 0 & \pi_{54} & \pi_{44} & 0 \\
\pi_{61} & \pi_{61} & 0 & 0 & 0 & 0
\end{bmatrix}
\cdot
\begin{bmatrix} \sigma \\ 0 \\ 0 \\ 0 \\ 0 \\ 0 \end{bmatrix}
=
\overset{x}{\begin{bmatrix} \pi_{11}\sigma_1 \\ \pi_{12}\sigma_1 \\ \pi_{13}\sigma_1 \\ 0 \\ 0 \\ \pi_{61}\sigma_1 \end{bmatrix}}
,
\overset{y}{\begin{bmatrix} \pi_{12}\sigma_2 \\ \pi_{11}\sigma_2 \\ \pi_{13}\sigma_2 \\ 0 \\ 0 \\ -\pi_{61} \end{bmatrix}}
\tag{58}
$$

for uniaxial crystals $N_1 = N_2 = N_o$

and $\qquad\qquad N_3 = N_e$

The change in index for a stress along the 1 direction (x) is given by

$$
\left.
\begin{aligned}
\Delta N_1 &= -\frac{1}{2}(N_1)^3 \, \Delta B_1 = -\frac{1}{2}(N_1)^3 \, \pi_{11}\sigma_1 \\[2mm]
\Delta N_2 &= -\frac{1}{2}(N_2)^3 \, \Delta B_2 = -\frac{1}{2}(N_2)^3 \, \pi_{12}\sigma_1 \\[2mm]
\Delta N_3 &= -\frac{1}{2}(N_3)^3 \, \Delta B_3 = -\frac{1}{2}(N_3)^3 \, \pi_{13}\sigma_1
\end{aligned}
\right\}
\tag{59}
$$

77

The change in index for a stress along the 2 direction (y) is given by

$$\left.\begin{array}{l} \Delta N_1 = -\frac{1}{2}(N_1)^3 \Delta B_1 = -\frac{1}{2}(N_1)^3 \pi_{12}\sigma_2 \\[2ex] \Delta N_2 = -\frac{1}{2}(N_2)^3 \Delta B_2 = -\frac{1}{2}(N_2)^3 \pi_{11}\sigma_2 \\[2ex] \Delta N_3 = -\frac{1}{2}(N_3)^3 \Delta B_3 = -\frac{1}{2}(N_3)^3 \pi_{13}\sigma_2 \end{array}\right\} \tag{60}$$

The change in index for a stress along the 3 direction is given by

$$\left.\begin{array}{l} \Delta N_1 = -\frac{1}{2}(N_1)^3 \Delta B_1 = -\frac{1}{2}(N_1)^3 \pi_{31}\sigma_3 \\[2ex] \Delta N_2 = -\frac{1}{2}(N_2)^3 \Delta B_2 = -\frac{1}{2}(N_2)^3 \pi_{32}\sigma_3 \\[2ex] \Delta N_3 = -\frac{1}{2}(N_3)^3 \Delta B_3 = -\frac{1}{2}(N_3)^3 \pi_{33}\sigma_3 \end{array}\right\} \tag{61}$$

Using the coordinate system, $1 = x$, $2 = y$, $3 = z$ and $\sigma = \sigma_1$, $\sigma_2 = \sigma_3 = 0$, and $N_1 = N_2 = N_o$ and $N_3 = N_e$, we obtain

$$N_1 = N_1{}^o + \Delta N_1 = N_1{}^o - \frac{1}{2}(N_1{}^o)^3 \pi_{11}\sigma_1 = N_o - \frac{1}{2}(N_o)^3 \pi_{11}\sigma_1 \tag{62a}$$

$$N_2 = N_2{}^o + \Delta N_2 = N_2{}^o - \frac{1}{2}(N_2{}^o)^3 \pi_{12}\sigma_1 = N_o - \frac{1}{2}(N_o)^3 \pi_{12}\sigma_1. \tag{62b}$$

Using the coordinate system, $3 = x$, $1 = y$, $2 = z$, $\sigma = \sigma_3$, $\sigma_1 = \sigma_2 = 0$, we obtain

$$N_1 = N_1{}^o - \frac{1}{2}(N_1{}^o)^3 \pi_{31}\sigma_3 = N_o - \frac{1}{2}(N_o)^3 \pi_{31}\sigma_3 \tag{63a}$$

$$N_3 = N_3{}^o - \frac{1}{2}(N_3{}^o)^3 \pi_{33}\sigma_3 = N_e - \frac{1}{2}(N_e)^3 \pi_{33}\sigma_3. \tag{63b}$$

Thus with two sample orientations, it is possible to measure four stress optical constants. In the next section we apply these results to the measurement of the elasto-optic constants.

D. FABRY-PEROT EFFECTS IN ELASTO-OPTIC MEASUREMENTS

When a high index slab of material is used in an elasto-optic stress measuring machine the effects of multiple beam interference must be taken into consideration. In this case the vertical axis becomes the parallel axis and the horizontal axis becomes the perpendicular axis. It can be shown that the complex transmission coefficients for the parallel and perpendicular polarizations after passing through the slab are given by

$$t_\parallel = \frac{4\,N_\parallel}{(N_\parallel + 1)^2} \cdot \frac{1}{1 - \left(\dfrac{N_\parallel - 1}{N_\parallel + 1}\right)^2 \exp\left(- i\,\dfrac{4\pi}{\lambda_o}\,N_\parallel\,T\right)} \tag{64a}$$

and

$$t_\perp = \frac{2\,N}{(N_\perp + 1)^2} \cdot \frac{1}{1 - \left(\dfrac{N_\perp - 1}{N_\perp + 1}\right)^2 \exp\left(- i\,\dfrac{4\pi}{\lambda_o}\,N_\perp\,T\right)} \cdot \tag{64b}$$

If the force is applied parallel to the parallel axis (vertical), then the total index is

$$N_\parallel = N_o - \frac{1}{2}\,(N_o)^3\,\pi_{11}\sigma_1, \text{ and } N_\perp = N_o - \frac{1}{2}\,(N_o)^3\,\pi_{12}\sigma_1 \tag{65a}$$

for propagation along the N_e axis, with stress along the N_o axis

and

$$N_\parallel = N_o - \frac{1}{2}\,(N_o)^3\,\pi_{31}\sigma_3, \text{ and } N_\perp = N_e - \frac{1}{2}\,(N_e)^3\,\pi_{33}\sigma_3 \tag{65b}$$

for propagation along the N_o axis, with stress along the N_e axis.

Using Equations 65(a) and 65(b) in Equations (64a) and (64b) we obtain for propagation along the N_e axis, with stress applied along the N_o axis,

$$t_\parallel = \frac{4(N_o - \frac{1}{2}(N_o)^3 \pi_{11}\sigma_1)}{(N_o - \frac{1}{2}(N_o)^3 \pi_{11}\sigma_1)^2} \cdot \frac{1}{1 - \left(\dfrac{N_o - \frac{1}{2}(N_o)^3 \pi_{11}\sigma_1 - 1}{N_o - \frac{1}{2}(N_o)^3 \pi_{11}\sigma_1 + 1}\right)^2 \exp\left[-i \frac{4\pi}{\lambda_o}(N_o - \frac{1}{2}(N_o)^3 \pi_{11}\sigma_1)T\right]} \tag{66a}$$

$$t_\perp = \frac{4(N_o - \frac{1}{2}(N_o)^3 \pi_{12}\sigma_1)}{(N_o - \frac{1}{2}(N_o)^3 \pi_{12}\sigma_1)^2} \cdot \frac{1}{1 - \left(\dfrac{N_o - \frac{1}{2}(N_o)^3 \pi_{12}\sigma_1 - 1}{N_o - \frac{1}{2}(N_o)^3 \pi_{12}\sigma_1 + 1}\right)^2 \exp\left[-i \frac{4\pi}{\lambda_o}(N_o - \frac{1}{2}(N_o)^3 \pi_{12}\sigma_1)T\right]} \cdot \tag{66b}$$

and for propagation along the N_o axis with stress applied along the N_e axis

$$t_\parallel = \frac{4(N_o - \frac{1}{2}(N_o)^3 \pi_{31}\sigma_3)}{(N_o - \frac{1}{2}(N_o)^3 \pi_{31}\sigma_3)^2} \cdot \frac{1}{1 - \left(\dfrac{N_o - \frac{1}{2}(N_o)^3 \pi_{31}\sigma_3 - 1}{N_o - \frac{1}{2}(N_o)^3 \pi_{31}\sigma_3 + 1}\right)^2 \exp\left[-i \frac{4\pi}{\lambda_o}(N_o - \frac{1}{2}(N_o)^3 \pi_{31}\sigma_1)T\right]} \tag{67a}$$

$$t_\perp = \frac{4(N_e - \frac{1}{2}(N_e)^3 \pi_{33}\sigma_3)}{(N_e - \frac{1}{2}(N_e)^3 \pi_{33}\sigma_3)^2} \cdot \frac{1}{1 - \left(\dfrac{N_e - \frac{1}{2}(N_e)^3 \pi_{33}\sigma_3 - 1}{N_e - \frac{1}{2}(N_e)^3 \pi_{33}\sigma_3 + 1}\right)^2 \exp\left[-i \frac{4\pi}{\lambda_o}(N_e - \frac{1}{2}(N_e)^3 \pi_{33}\sigma_3)T\right]} \tag{67b}$$

Taking the ratios $t_\parallel/t_\perp$ for Equations (66) and (67) respectively we can obtain expressions of the form

$$t_\parallel / t_\perp = \tan \psi \, e^{i\Delta} \qquad\qquad (68)$$

where the ten factors $\tan \psi$ and $e^{i\Delta}$ can be separated. These two variables Δ and ψ can be measured in an ellipsometer and an iterative calculation of Equation (68) can be made to obtain the best fit to the Δ, ψ data. This calculation can be done for both stressed and unstressed samples to deduce the elasto-optic constants. The calculation of the sensitivity of this method is quite complicated and is best done using a computer.

An advantage to this method is that it can be applied to a very small region of the sample using microspot optics.

E.   OPTICAL MEASUREMENTS

During the last quarter of this program a first attempt was made to make an ellipsometric measurement of the elasto-optic constant of materials using the anisotropic transmission ellipsometric technique. In this experiment, the sample must be held in such a way as to provide alignment in x,y,z coordinates as well as precise rotation about three orthogonal axes. To accomplish this, an x,y,z translation stage was assembled and coupled to a Rudolph research ellipsometer. The rotations were provided by a set of commercial mounts. The stress was applied mechanically by means of a precision screw (micrometer movement).

Our intention was to measure the stress optic coefficient by a relative method, i.e., the same stress is applied to the new material to be measured at the same time as it is applied to a known sample, e.g., fused quartz. We found this method to be unusable in the laboratory because the experiment is extremely critical with regard to alignment. In particular, shifts of approximately 10^{-3} radians in angular position cannot be tolerated experimentally.

We are currently redesigning the sample mounts to include stronger stages as well as a provision to directly measure the stress by means of a load cell. In addition, we plan to exert the pressure pneumatically rather than by a mechanical screw so that unnecessary torques can be avoided.

SECTION 7

CONCLUSIONS AND RECOMMENDATIONS

A real need exists for improved materials for many applications of interest to DoD including electro-optic and acousto-optic modulators, switches, tunable filters, as well as for new devices based on principles such as degenerate four-wave mixing. Utilization of four-wave mixing techniques in practical devices could greatly increase optical system integration by expanding the possibilities of amplification, convolution, correlation, and pulse compression. Electro-optic and acousto-optic devices are essentially materials limited; currently available materials are inefficient in terms of power required and often absorb light in the spectral regions where operation is desired. New materials are also needed for surface acoustic wave (SAW) devices where the lack of materials with large coupling coefficients and inherent temperature stability has limited the bandwidth of these devices and makes them unsuitable for many microwave applications.

The primary objective of this program was to search for new improved materials. We have succeeded in finding a new electro-optic infrared-transmitting material, $CdIn_2Te_4$, with more than an order of magnitude increase in its longitudinal EO coefficient over known IR materials. This material has great potential in the development of far infrared modulators and tunable spectral filters since it allows an engineering margin in the voltage requirements of driver chips. In the Hughes longitudinal electro-optic tunable filter (LEOTF), the voltage requirements are reduced by a factor of 20, compared to the previously selected material $AgGaS_2$. This is a result of the higher refractive indices of $CdIn_2Te_4$ and their effect on the electro-optic figure of merit, i.e., n^3r_{41}. This filter design now can be extended into the far infrared using state-of-the-art driver chips.

The discovery of a large electro-optic coefficient as we originally predicted in this material gives credibility to our structural analog approach. An important factor in this pursuit has been the ability to measure low-frequency dielectric constants in polycrystalline samples, thus saving time required for single crystal development. The extension of this to acousto-optic and non-linear properties has not been as direct. Certainly, the large EO coefficient indicates the possibility of a large non-linear coefficient

83

since it is related to the ionic contribution to the EO coefficient. In addition, a look at materials properties shows the possibility of finding materials with large AO figures of merit among the interesting materials falling into this group. What is missing is a characterization technique which can be easily and meaningfully carried out on polycrystalline samples, which is also a strong indicator of large values of those properties of interest.

Our investigation for such evaluation techniques has led to the development of a very promising technique for measurement of stress-optic coefficients: Anisotropic Transmission Ellipsometry. We were not able to complete the construction and testing of this apparatus during the course of this program. We plan to evaluate this technique in the near future using small single crystal samples and will make the results known to the Air Force.

We recommend that the work which commenced during the course of this investigation be further pursued by the Air Force and other agencies of the Government. This work has opened the door on new ideas and approaches to the discovery and development of new materials for the applications mentioned above. We enter that door with a greater degree of confidence, having valid proof of our approach. There is still a lot of materials work to be pursued as well. As becomes obvious in this study, problems remain in the synthesis of some of the new compounds which must be resolved prior to approaching growth of single crystals. The laboratory work must be accompanied by theoretical work, as demonstrated by this program, in order to understand the selection and prediction of new materials and their pertinent optical properties. In addition, all the accrued knowledge must be used to develop efficient diagnostic procedures for evaluating and/or predicting those properties in materials which are of prime concern for these applications.

REFERENCES

1. DARPA Contract MDA 903-78-C-0180, 1 May 78 - 30 June 80.

2. R..W. Dixon, J. Appl. Phys. 38, 5149-5153 (1967).

3. R.W. Dixon and M. G. Cohen, Appl. Phys. Lett. 8, 205-206 (1966).

4. D.A. Pinnow, IEEE J Quantun Electron, QE-6 [4] 223-238 (1970).

5. A.L. Gentile, S.R. Sashital, N.R. Kyle et al., "New Materials for Infrared Transmitting Electro-optic Filters," Final Technical Report, Contract MDA 903-78-C-0180, August 1980, sponsored by Defense Advanced Projects Research Agency (Order No. 3519).

6. L.I. Berger and V.D. Prochukhan, "Ternary Diamond-Like Semiconductors," Consultants Bureau (1969).

7. C.-C. Shih and A. Yariv, Phys. Rev. Lett. 44, 281-284 (1980).

8. J.H. Gladstone and T.P. Dale, Philos. Trans. R. Soc. London 153, 337 (1864)

9. S.H. Wemple and M. DiDomenico, Jr., J. Appl. Phys. 40, 735-752 (1969).

10. S.H. Wemple and M. DiDomenico, Jr. (unpublished), in D.A. Pinnow, op. cit.

11. G.W. Roland, J.D. Feichtner, M. Rubenstein, and W.E. Kramer, "The Crystal Growth and Application of Sulfosalt Materials" Report AFML-TR-75-172, (November 1975).

12. L. Thomassen et al., J. Electrochem. Soc. 110, 1127 (1963).

13. A. Borshchevsky, Private Communication, 1980.

14. L.A. Palatnik and E.K. Belova, Izv Akad. Nauk SSSR, Neorgan. Mater. 3, 2194 (1967).

15. A.L. Gentile and O.M. Stafsudd, Mat. Res. Bull. 9, 105-116 (1974)

16. G.D. Boyd, E. Buehler and F.G. Story, Appl Phys. Letters 18, 301-304 (1971).

17. G.D. Boyd, W.B. Gandrud and E. Buehler, Appl. Phys. Letters 18, 446-448 (1971).

18. J.C. Phillips, Phys. Rev. Lett. 20, 550 (1968).

19. J.A. Van Vechten, Phys. Rev. Lett. 182, 891 (1969), 187, 1007 (1969).

20. D.S. Chemla, Phys. Rev. Lett. 26, 1441-1444 (1971).

APPENDIX

DERIVATION OF THE ANISOTROPIC OPTICAL PHASE SHIFT Δ AND THE TRANSMISSION
RATIO TANψ FOR MULTIPLE BEAM INTERFERENCE IN A PLATE

The complex transmission factor for a wave normally incident on a plate
with parallel faces is given by

$$t = \frac{\tau}{1 - Re^{i\delta}} \tag{1}$$

where $\tau = 4n/(n + 1)^2$ is the power transmission coefficient at the first sur-
face and $R = (n - 1)/(n + 1)^2$ is the power reflection coefficient at the first
surface and $\delta = 4\pi/\lambda_o \, nT$ is the double transit optical phase shift for the
wave and n,t and λ_o are the refractive index, the sample thickness, and the
wavelength, respectively.

From this expression the ratio of the complex transmission factors for
an anisotropic medium is written as

$$t_{\parallel}/t_{\perp} = \frac{\tau_{\parallel}}{\tau_{\perp}} \frac{1 - R_{\perp} e^{i\delta_{\perp}}}{1 - R_{\parallel} e^{i\delta_{\parallel}}} \tag{2}$$

where

$$\tau_{11} = \frac{4\, n_{11}}{(n_{11}+1)^2} \quad , \quad R_{11} = \left(\frac{n_{11}-1}{n_{11}+1}\right)^2 \quad , \quad \tau_{\perp} = \frac{4\, n_{\perp}}{(n_{\perp}+1)^2}$$

and

$$R_{\perp} = \left(\frac{n_{\perp} - 1}{n_{\perp} + 1}\right)^2$$

represent the tensor refractive index values for a system in which the optic
axis of the sample is aligned either parallel or perpendicular to one of the
incident optical polarization. This is a principal coordinate geometry system

and relatively easy to analyze. Other orientations are much more difficult. The ratio $t_{\parallel}/t_{\perp}$ can be represented by an amplitude and a phase factor with the form

$$\text{Tan}\psi \; e^{i\Delta} = \frac{t_{\parallel}}{t_{\perp}} = \frac{\tau_{\parallel}}{\tau_{\perp}} \; \frac{1 - R_{\perp}\text{Cos}\delta_{\perp} - i\,R_{\perp}\text{Sin}\delta_{\perp}}{1 - R_{\parallel}\text{Cos}\delta_{\parallel} - i\,R_{\parallel}\text{Sin}\delta_{\parallel}} \; . \tag{3}$$

With the substitution $A = \tau_{\parallel}/(\tau_{\perp}\,\text{Tan}\psi)$ this can be expanded to

$$(\text{Cos}\Delta + i\,\text{Sin}\Delta)(1 - R_{\parallel}\text{Cos}\delta_{\parallel} - i\,R_{\parallel}\text{Sin}\delta_{\parallel}) = (A - AR_{\perp}\text{Cos}\delta_{\perp} - i\,AR_{\perp}\text{Sin}\delta_{\perp}) \tag{4}$$

Cross-multiplying and collecting terms, the real and the imaginary terms yield 2 equations:

$$\text{Cos}\Delta - \text{Cos}\Delta R_{\parallel}\text{Cos}\delta_{\parallel} + \text{Sin}\Delta R_{\parallel}\text{Sin}\delta_{\parallel} = A(1 - R_{\perp}\text{Cos}\delta_{\perp}) \tag{5a}$$

and

$$\text{Cos}\Delta R_{\parallel}\text{Sin}\delta_{\parallel} - \text{Sin}\Delta + \text{Sin}\Delta R_{\parallel}\text{Cos}\delta_{\parallel} = -AR_{\perp}\text{Sin}\delta_{\perp} \; . \tag{5b}$$

Dividing Equations (5b) into (5a) eliminates the A term which contains Tanψ

$$\frac{\text{Cos}\Delta - \text{Cos}\Delta R_{\parallel}\text{Cos}\delta_{\parallel} + \text{Sin}\Delta R_{\parallel}\text{Sin}\delta_{\parallel}}{\text{Cos}\Delta R_{\parallel}\text{Sin}\delta_{\parallel} - \text{Sin}\Delta + \text{Sin}\Delta R_{\parallel}\text{Cos}\delta_{\parallel}} = \frac{1 - R_{\perp}\text{Cos}\delta_{\perp}}{- R_{\perp}\text{Sin}\delta_{\perp}} \; . \tag{6}$$

Again cross multiplying and collecting terms for CosΔ and SinΔ we obtain

$$\frac{\text{Sin}\Delta}{\text{Cos}\Delta} = \text{Tan}\Delta = - \frac{R_{\perp}R_{\parallel}\text{Sin}(\delta_{\perp} - \delta_{\parallel}) - R_{\perp}\text{Sin}\delta_{\perp} - R_{\parallel}\text{Sin}\delta_{\parallel}}{R_{\perp}R_{\parallel}\text{Cos}(\delta_{\perp} - \delta_{\parallel}) - R_{\perp}\text{Cos}\delta_{\perp} - R_{\parallel}\text{Cos}\delta_{\parallel} + 1} \tag{7}$$

for an isotropic medium $\delta_{\perp} = \delta_{\parallel}$ and $\text{Tan}\Delta \equiv 0$.

Using Equation (5b) we derive an expression for Tanψ

$$\text{Tan}\psi = \frac{\tau_{\parallel}}{\tau_{\perp}} \; \frac{R_{\perp}\text{Sin}\delta_{\perp}}{\text{Cos}\Delta R_{\parallel}\text{Sin}\delta_{\parallel} - \text{Sin}\Delta + \text{Sin}\Delta R_{\parallel}\text{Cos}\delta_{\parallel}} \tag{8}$$

or

$$\text{Tan}\psi = \frac{\tau_{\parallel}}{\tau_{\perp}} \frac{R_{\perp}\text{Sin}\delta_{\perp}}{R_{\parallel}\text{Sin}(\Delta + \delta_{\parallel}) - \text{Sin}\Delta} \, , \qquad (8a)$$

for an isotropic medium $R_{\perp} = R_{\parallel}$, $\tau_{\parallel} = \tau_{\perp}$, $\delta_{\perp} = \delta_{\parallel}$, $\Delta = 0$ and $\text{Tan}\psi \equiv 1$.
Thus the transmission ratio is 1 as expected.

These expressions can be written in terms of the refractive index $n_{\perp}$ and
$n_{\parallel}$ and the sample thickness T as shown

$$\text{Tan}\Delta = \frac{\left(\frac{n_{\perp}-1}{n_{\perp}+1}\right)^2\left(\frac{n_{\parallel}-1}{n_{\perp}+1}\right)^2\text{Sin}\left(\frac{4\pi}{\lambda_0}T[n_{\perp}-n_{\parallel}]\right) - \left(\frac{n_{\perp}-1}{n_{\perp}+1}\right)^2\text{Sin}\frac{4\pi}{\lambda_0}n_{\perp}T + \left(\frac{n_{\parallel}-1}{n_{\parallel}+1}\right)^2\text{Sin}\frac{4\pi}{\lambda_0}n_{\parallel}T}{\left(\frac{n_{\perp}-1}{n_{\perp}+1}\right)^2\left(\frac{n_{\parallel}-1}{n_{\parallel}+1}\right)^2\text{Cos}\left(\frac{4\pi}{\lambda_0}T[n_{\perp}-n_{\parallel}]\right) - \left(\frac{n_{\perp}-1}{n_{\perp}+1}\right)^2\text{Cos}\frac{4\pi}{\lambda_0}n_{\perp}T - \left(\frac{n_{\parallel}-1}{n_{\parallel}+1}\right)^2\text{Cos}\frac{4\pi}{\lambda_0}n_{\parallel}T + 1} \qquad (9a)$$

and

$$\text{Tan}\psi = \frac{\left[\frac{4\,n_{\parallel}}{(n_{\parallel}+1)^2}\right]\left(\frac{n_{\perp}-1}{n_{\perp}+1}\right)^2\text{Sin}\frac{4\pi}{\lambda_0}n_{\perp}T}{\left[\frac{4_{\perp}n}{(n_{\perp}+1)^2}\right]\left(\frac{n_{\parallel}-1}{n_{\parallel}+1}\right)^2\text{Sin}\left(\Delta + \frac{4\pi}{\lambda_0}T\,n_{\parallel}\right) - \text{Sin}\Delta} \qquad (9b)$$

For $n_{\perp} \stackrel{\sim}{\sim} n_{\parallel}$ if we let $n_{\perp} = \bar{n}$; $n_{\perp} - n_{\parallel} = \Delta\bar{n}$

$$\text{Tan}\Delta \approx \frac{\left(\frac{\bar{n}-1}{\bar{n}+1}\right)^4\text{Sin}\frac{4\pi}{\lambda_0}T\,\Delta\bar{n} - \left(\frac{\bar{n}-1}{\bar{n}+1}\right)^2\text{Sin}\frac{4\pi}{\lambda_0}\bar{n}\,T - \left[\text{Sin}\frac{4\pi}{\lambda_0}(\bar{n}-\Delta n)\,T\right]}{\left(\frac{\bar{n}-1}{\bar{n}+1}\right)^4\text{Cos}\frac{4\pi}{\lambda_0}T\,\Delta\bar{n} - \left(\frac{\bar{n}-1}{\bar{n}+1}\right)^2\text{Cos}\frac{4\pi}{\lambda_0}\bar{n}\,T + \left[\text{Cos}\frac{4\pi}{\lambda_0}(\bar{n}-\Delta n)\,T\right] + 1} \, . \qquad (10)$$

89

Using trigonometric identities, we get a simplified version of this equation suitable for evaluating small anisotropic samples:

$$\text{Tan}\Delta = \frac{\left(\frac{n-1}{n+1}\right)^4 \left(\text{Sin}\left(\frac{4\pi}{\lambda_o} T\Delta\bar{n}\right)\right) - \left(\frac{\bar{n}-1}{\bar{n}+1}\right)^2 \left(2\ \text{Cos}\left(\frac{2\pi}{\lambda_o} T\Delta\bar{n}\right)\cdot\ \text{Sin}\left(\frac{2\pi}{\lambda_o} T\Delta\bar{n}\right)\right)}{\left(\frac{n-1}{n+1}\right)^4 \left(\text{Cos}\left(\frac{4\pi}{\lambda_o} T\Delta\bar{n}\right)\right) - \left(\frac{\bar{n}-1}{\bar{n}+1}\right)^2 \left(2\ \text{Cos}\left(\frac{4\pi}{\lambda_o} T\Delta\bar{n}\right)\text{Cos}\left(\frac{2\pi}{\lambda_o} T\Delta\bar{n}\right)\right) + 1} \quad . \tag{11}$$

For example, for $\Delta n = 10^{-3}$ $\lambda = 10^{-6}$ n $T = 5 \times 10^{-3}$ m we get a very large phase shift, $\delta = 2\pi/\lambda_o$, T $\Delta n = 6.28/10^{-6} \times 5 \times 10^{-3} = 30$. This means that an anisotropy $\Delta n = 0.001$ produces a 30 rad phase shift in a sample 5 mm thick. In a 1-mm-thick sample, it would produce a phase shift of ~6 rad (=360°). Because there is no simple way of approximating these equations, even in the presence of small anisotropy (0.0001 anisotropy produces 0.628 rad or 36° in a 1 mm sample), we will have to evaluate the anisotropy in each sample before we can evaluate the change in anisotropy caused by stress using this method. This could be done using Equation (9b) and the experimentally measured value of ψ and Δ. It is assumed that the thickness of the sample can be measured with great precision. A thickness error of ΔT produces a phase shift of $4\pi/\lambda_o$ n ΔT. For n = 2.54 and $\Delta T = 10^{-6}$ m this becomes 30 rad. Thus an error of 1 µm in measuring the sample thickness can give rise to a 30 rad error in the calculation of the phase angle Δ. A precision of 100 A produces a phase error of 0.3 rad or 18° and a precision of 1 A produces a phase error of 0.003 rad or 0.18°. (The precision of an ellipsometer is ±0.1°.)

Because of the complexity of Equations (9a) and (9b) it is possible that only one set of values $n_{\parallel}$, $n_{\perp}$ and T will allow a theoretical calculation of Δ, ψ which matches the experimental Δ, ψ values. However, the chances of solving the equations improves dramatically as one fixes either of the indices $n_{\perp}$ or $n_{\parallel}$ or the thickness with greater precision.

If the wavelength of the apparatus is changed,then another set of
equations is obtained and again numerous theoretical fittings to the data are
possible. By comparing these results in tabular form,only one set of $n_\perp n_\parallel$ and
T will agree if the medium is nondispersive. If it is dispersive only one
set of thicknesses will agree for all wavelengths. Thus this method can be
used to evaluate the natural anisotropy in elasto-optic materials and then
the stress- or strain-induced anisotropy as an increment in the natural
anisotropy. This is not a simple method theoretically,but it should be
capable of extremely high precision because of its ultrahigh sensitivity to
phase angle shifts. In comparison the standard interferometric methods
require a high stability optical system and are good only to a tenth of a
fringe or 3°.

MISSION
of
Rome Air Development Center

RADC plans and executes research, development, test and selected acquisition programs in support of Command, Control Communications and Intelligence (C^3I) activities. Technical and engineering support within areas of technical competence is provided to ESD Program Offices (POs) and other ESD elements. The principal technical mission areas are communications, electromagnetic guidance and control, surveillance of ground and aerospace objects, intelligence data collection and handling, information system technology, ionospheric propagation, solid state sciences, microwave physics and electronic reliability, maintainability and compatibility.

END

FILMED

6-84

DTIC